

INVESTIGATION OF OPTICAL RESIDUAL ABSORPTION IN GRAPHENE

A THESIS SUBMITTED TO
THE GRADUATE SCHOOL OF ENGINEERING AND SCIENCE
OF BILKENT UNIVERSITY
IN PARTIAL FULFILMENT OF THE REQUIREMENTS FOR
THE DEGREE OF
MASTER OF SCIENCE
IN
PHYSICS

By
Zeinab Eftekhari
February 2018

INVESTIGATION OF OPTICAL RESIDUAL ABSORPTION IN GRAPHENE

By Zeinab Eftekhari

February 2018

We certify that we have read this thesis and that in our opinion it is fully adequate, in scope and in quality, as a thesis for the degree of Master of Science.

Oğuz Gülseren (Advisor)

Coşkun Kocabaş (Co-advisor)

Alpan Bek

Mehmet Özgür Oktel

Approved for the Graduate School of Engineering and Science:

Ezhan Karaşan
Director of the Graduate School

ABSTRACT

INVESTIGATION OF OPTICAL RESIDUAL ABSORPTION IN GRAPHENE

Zeinab Eftekhari

M.Sc. in Physics

Advisor: Oğuz Gülseren

February 2018

Graphene, a 2-dimensional crystal of carbon, can absorb 2.3% of light over a very broad spectrum. Doped graphene, however has a gap in optical absorption due to the Pauli blocking principle. For doped graphene, the interband optical transitions with energy less than $2E_F$ are not allowed, therefore the consequent optical absorption is expected to fall down to zero for energies below $2E_F$ threshold. In this thesis, we investigated the optical residual absorption of graphene in Pauli-blocked region. Optical absorption of the monolayer graphene transferred on transparent substrates was analyzed via optical spectroscopy. We used electrostatic and chemical doping methods to shift Fermi energy of graphene. The observed residual absorption of 0.5% which is due to chemical impurities reduced slightly by increasing doping level.

Keywords: graphene, optical residual absorption, electrolyte gating, quantum absorption of 2Ds.

ÖZET

GRAFENDE OPTİK ARTIK SOĞRULMANIN İNCELENMESİ

Zeinab Eftekhari

Fizik, yüksek lisans

Tez Danışmanı: Oğuz Gülseren

Şubat 2018

2-boyutlu karbon kristali olan graphen, çok geniş bir spektrumda ışığın % 2,3' ünü soğurabilir. Bununla birlikte, katkılı grafenin, Pauli bloklama ilkesinden dolayı optik soğurma aralığı vardır. Katkılı grafende 2EF'den daha düşük enerjili bantlararası optik geçişlere izin verilmemektedir; bu nedenle, sonuçta meydana gelen optik soğurmanın, 2EF eşiğinin altındaki enerjiler için sıfıra düşmesi beklenmektedir. Bu tez çalışmasında, Pauli bloklu bölgede grafenin optik artık soğurmasını araştırdık. Şeffaf alttaşlar üzerine transfer edilmiş tek tabakalı grafenin optik soğurması optik spektroskopi ile analiz edildi. Grafenin Fermi enerjisini kaydırmak için elektrostatik ve kimyasal katkılama yöntemlerini kullandık. Kimyasal safsızlıklara bağlı olarak gözlemlenen % 0,5'lik artık soğurma, katkılama seviyesinin artmasıyla hafifçe azalmıştır.

Anahtar sözcükler: grafen, optik artık soğurma, elektrolit kapılama, 2Dlerin kuantum soğurulması.

Acknowledgement

I would like to fully appreciate my advisor, Prof. Oğuz Gülseren, for his help and timely guidance. I would like to express my deepest gratitude to my co-advisor, Prof. Coşkun Kocabaş for introducing me to the exciting area of graphene and giving me an opportunity to do experimental research in his lab. It would not be possible to finish this thesis without his insightful opinion and knowledge.

I gratefully acknowledge the valuable time and constructive comments of my defense committee members; Prof. Alpan Bek and Prof. Mehmet Özgür Oktel.

I am thankful to Prof. Sinan Balcı, Dr. Osman Balcı and Dr. Nurbek Kakenov for their advice, inspiration and support. I am so grateful to Prof. Ekmel Ozbay and Dr. Alireza Rahimi Rashed for allowing me to perform FTIR microscopy studies in NANOTAM.

I would also express my great appreciation to Said Ergöktaş and Hasan Burkay Uzlu for training me on the usage of the equipment in the lab. I would like to thank Dr. Evgenia Kovalska, Prof. Eda Goldenberg, Dr. Pınar Köç, Doolos Aibek Uulu and Uğur Demirkol.

I am also thankful to the faculty and the staff of Advanced Research Laboratory, UNAM and Department of Physics for providing me delightful atmosphere throughout my study.

Finally, I would like to thank my loving family, specially my husband Wiria for the constant support and encouragement. To them I dedicate this thesis.

In dedication to my loving family

Contents

1 Introduction	1
2 Optics in 2D materials	3
2.1 Quantum wells band structure	4
2.2 Optical absorption of quantum wells	8
2.3 Quantum Optical absorption of InAs membrane.....	10
3 Optical Properties of Graphene	13
3.1 Electronic structure of graphene	13
3.2 Doping of graphene	16
3.3 Optical properties of graphene.....	18
3.4 Synthesis of graphene	25
3.5 Transfer procedure.....	28
3.6 Optical response of highly doped graphene.....	31
4 Optical residual absorption of graphene	38
4.1 Introduction.....	38
4.2 Simulation of monolayer graphene.....	40
4.3 Experimental results and discussion.....	46
5 Conclusion	57
6 Bibliography	59

List of Figures

Figure 2.1 Electron levels of materials generated from four valent atoms such as carbon or binary compounds like Indium Arsenide schematics. S and p orbitals turn into bonding and antibonding states by hybridization and induce valence and conduction bands of the crystal.	4
Figure 2.2 Schematic diagram of band structure of direct gap III-V semiconductors near to the center of Brillouin zone.....	6
Figure 2.3 First three energy levels and corresponding wave functions of an infinite potential well of width L_z	8
Figure 2.4 The first and second allowed interband optical transitions in accordance with selection rules in a quantum well. However electrons and holes have discrete energy levels in the quantum well, they can move freely in the x-y plane of the well and have kinetic energy associated with the free motion. Therefore the total energy can be determined by following:	9
Figure 2.5 The step like absorption coefficient of an infinite quantum well of width L_z compared to the 3D case.	10
Figure 2.6 Experimental absorption of InAs QMs of different thicknesses at room temperature. The magnitude of quantum absorptance A_Q for each step is 1.6% and are shown by dashed lines. The A_{en-hn} indicates the absorption corresponding to the interband transition from nth hole state to the nth electron state [8].	11
Figure 3.1 schematic of lattice structure of graphene (a) Honeycomb crystal structure of graphene with a unit cell consisting of two carbon atoms.	

(b)The first Brillion zone of graphene with hexagonal shape where all corners of the hexagon are Dirac points.....	14
Figure 3.2 Electrolyte gating method of graphene. Applied gate voltage generates an electrostatic potential difference between the gold electrode and the graphene. Fermi energy is shifting by increasing charge carriers through electric field.	17
Figure 3.3 Graphene’s Dirac cones in three different cases. P-doped graphene is obtained by introducing holes to the graphene and therefore, Fermi energy shifted down. In the pristine graphene, Fermi level is at the Dirac point. The n-doped graphene is electron injected and Fermi energy is shifted up.	18
Figure 3.4 Wide-range optical response of graphene illustrated from visible to microwave spectrum. Graphene absorbs 2.3% of light at visible-near infrared region in which interband transitions arise from high energy photons. However, the absorption reaches 50% due to intraband transitions for low energy photons at terahertz and microwave area....	19
Figure 3.5 Interband transitions. (a) A photon with energy of $2E_F$ or more is absorbed by an electron exciting it from valence band to conduction band. (b) Optical transitions for energies less than $2E_F$ are blocked.....	20
Figure 3.6 Modeled real and imaginary parts of conductivity of graphene at different temperatures. Both parts are temperature dependent.	22
Figure 3.7 Optical spectrum of graphene at different Fermi energies in visible range. (a) Transmittance of graphene is about 97.7% in visible range (b) absorption spectrum of graphene is about 2.3% for energy photons of $2E_F$. Therefore, by increasing Fermi energy, transition of photons with less energy is blocked.	23

Figure 3.8 Low energy photons in the conduction band can excite electrons within the band called intraband transition.	24
Figure 3.9 Intraband conductivity (a) Real part of Drude conductivity at different Fermi energies. (b) Imaginary Drude conductivity of different Fermi energies.	25
Figure 3.10 (a) Quartz chamber is placed in the furnace and the temperature of furnace can rise up to 1070 degrees. (b) Cu foils are cut and arranged on the holder.....	26
Figure 3.11 (a) Vacuum Gauge showing that chamber is pumped down to a vacuum of 6 mTorr. (b) Mass flow controllers showing flow amount of hydrogen and methane.	27
Figure 3.12 Graphene transfer process. (a) Photoresist (PR) on CVD-deposited graphene on Cu. (b) The baked sample in the etchant to remove Cu. (c) Graphene on PR placed on the polyethylene substrate and heated on a hotplate. (d) Graphene on polyethylene where the PR is removed by acetone.....	29
Figure 3.13 Graphene transferred on PVC by lamination. (a) Lamination machine used to laminate CVD graphene on the PVC substrate. (b) Laminated graphene where graphene is between the PVC and Cu. (c) Cu removed by iron chloride to leave graphene on PVC. The tapes used to avoid Cu etching on the sides to take contact from graphene. (d) The conductance of graphene on PVC in kilo ohm.....	30
Figure 3.14 schematic of device structure. The device is composed of gold electrode, graphene on a substrate and ionic liquid in between as a gating medium. By applying voltage, ionic liquid gets polarized generating ELD and induce electric field.....	32

Figure 3.15 The FTIR spectrometer setup.....	33
Figure 3.16 To Find the Charge neutrality point (a) Capacitance and (b) Resistance of graphene device vs gate voltage is measured.	34
Figure 3.17 Normalized transmittance of graphene device at visible for (a)electron doping regime and (b)hole doping regime of different Fermi energies.	35
Figure 3.18 Extracted Fermi energies of different gate voltages from cutoff wavelength.	36
Figure 3.19 Differential transmittance of graphene device at near and mid infrared for electron doping regime.	36
Figure 3.20 Terahertz transmittance spectrum of graphene device at electron doping regime.....	37
Figure 4.1 Schematic of optical response of monolayer graphene with conductivity of σ sandwiched between two dielectric media with dielectric constants of ϵ_1 and ϵ_2 . Forward and backward propagating electromagnetic waves with field coefficients of a_1 , a_2 , b_1 and b_2 , respectively.	40
Figure 4.2 Optical response of free standing graphene at different fermi energies. (a) Transmittance of graphene is about 97.7% considering negligible reflectance yields 2.3% absorption. (b) Reflectance spectrum of graphene is inconsiderable and does not have significant effect on the graphene's absorption. (c) Absorption of graphene is about 2.3% in this region.....	44
Figure 4.3 Optical spectrum of graphene on a dielectric substrate with refractive index of $n = 1.5$. (a) 91.7% of transmittance is calculated which is decreased compared to the transmittance of free standing graphene.	

(b) Reflectance is increased to 6.7% and (c) Graphene's absorption is decreased to 1.57% due to refractivity of the substrate.	45
Figure 4.4 Absorption of graphene on quartz substrate for high energy photon region at different Fermi energies. Enhancement of absorption due to interband transitions near M point including excitonic effect is pronounced.	46
Figure 4.5 The examined sample is CVD grown graphene on quartz where, chemical doping (HNO_3 here) is exploited to shift Fermi energy of graphene. By exposing our sample to nitric acid, we can obtain p-doped graphene.	48
Figure 4.6 Simplified schematic of UV-Vis-NIR spectrophotometer. Light provided by source proceeds to monochromator and the narrow bandwidth outgoing beam of light splits into two beams by beam splitter. One of the beams is transmitted via the reference and the other passes through the sample. The ratio intensity of beams after detection by photo diodes is processed and the spectrum (transmittance vs wavelength) appears on display.	49
Figure 4.7 Transmission spectrum of graphene on quartz sample exposed to nitric acid. We took quartz as background and measured transmission of graphene. Then by nitric acid exposure in two steps of 1 and 3 minute, transmittance graphene was measured at different Fermi energies.	50
Figure 4.8 Normalized absorption of graphene at different Fermi energies. A finite residual absorption of 0.5% is measured which decreases slightly by increasing the doping level.	51
Figure 4.9 Transmittance spectrum of graphene. We took quartz as background and measured transmittance of graphene then exposed it to ammonia to observe transmission of graphene at higher wavelengths.	52

Figure 4.10	Normalized absorption of graphene at lower frequencies in NIR range. Fermi energy is shifting by chemical doping of ammonia to higher wavelengths while the absorption is almost constant and is around 1.7%. The optical residual absorption is 0.5% and is nearly consistent for different Fermi energies.	53
Figure 4.11	Extracted Fermi energies of chemically doped graphene. The hole-doped graphene by nitric acid indicates increasing the Fermi energy while the electron doped part shows the reduction of Fermi energies..	54
Figure 4.12	Absorption spectra of monolayer, 2layer and 3layer graphene versus energy. The inset shows the visible absorption of stacked layers of graphene.	55
Figure 4.13	Comparison between experimental absorption of graphene with the model at different Fermi energies.	56

Chapter 1

Introduction

Graphene as a two-dimensional (2D) material fascinated the scientific community for its fundamental physics and extensive applications. Graphene is made of one layer of carbon atoms with an optical absorption of about 2.3% and can be observed with bare eyes [1, 2]. Electronic band structure of graphene indicates the linear energy-momentum dispersion which results in massless Dirac fermions within Dirac approximation [3]. Graphene demonstrates extraordinary response in terms of light-matter interactions. Strong and broadband interactions of graphene with electromagnetic waves aid to the understanding of its unusual physics. Probing optical properties of graphene can be useful in the next-generation photonics and optoelectronic applications. In addition to unique absorption spectrum, graphene's Fermi level is highly tunable by electrostatic gating [4]. The optical absorption of graphene ensued from participation of inter-band and intra-band optical transitions and it can be modified by tuning the concentration of charge carriers through doping [5]. The shift of Fermi energy induced by doping blocks optical transitions due to Pauli's exclusion principle therefore we expect vanishing of optical absorption in Pauli blocking regime. However experimental data shows a considerable amount of residual absorption which can be due to impurities or many-body interactions [6].

In this thesis, we investigate optical residual absorption of graphene. It is crucial to first be able to observe and measure the optical residual absorption of graphene and then identify if it is due to graphene's intrinsic properties or coming from chemical impurities introduced to graphene during the growth and transfer processes. As it

mentioned before, graphene's optical absorption is 2.3% in at visible-NIR range theoretically, while the experimental results may show different amount. Therefore, our aim in this study is to reveal which factors contributes in graphene's absorption in this particular region.

First, a relevant introductory information about optical absorption of 2D materials is provided. Quantum optical absorption of indium arsenide quantum membranes as a 2D material model has been described which will be used in the analysis of our experimental data. Afterwards, electronic band structure of graphene, together with two mechanism that describe its optical absorption are introduced. Then, experiment's details of growth of graphene and the transfer process are demonstrated. Optoelectronic measurements rendered by optical spectroscopy are presented and discussed. The last chapter provides information about optical residual absorption of graphene. The physics behind the modeling has been demonstrated followed by the section of results. In chapter 4, another experiment is designed to measure the optical spectrum of chemically doped graphene. Finally, the fitting of the model to the experimental measurements is discussed.

Chapter 2

Optics in 2D materials

2-dimensional materials feature atomic thickness that induce quantum confinement effects. Charge carriers confined in one dimension give rise to unique optical properties in 2D materials. Optical absorption of 2D systems such III-V quantum wells has been studied to demonstrate that the optical absorption of 2Ds is quantized independent of their thickness. The thickness certainly should be very small compared to the effective Bohr radius to carriers remain confined. The quantized absorption of quantum well is showed in a stepwise manner which each step is $1.6 \pm 0.2\%$. The optical absorption of graphene as an atomically thin 2D material is about 2.3% in the visible range. In the case of graphene lied on a substrate, the optical absorption will be determined taking into account the refractive index of the substrate. When the correction factor associated with refractive index of substrate is applied, the absorption of graphene will be the same as quantum membranes absorption step. The comparison lead to the conclusion of a universal optical absorption for 2D materials.

2.1 Quantum wells band structure

The concept of quantum well was proposed by Esaki and Tsu in 1970 and it has turned out to have a significant impact on semiconductor physics. Quantum well's exotic optical properties made it an essential element for optoelectronic applications.

Quantum wells are made of a thin layer of semiconductor material sandwiched between two other layers which generate a potential well with infinite barriers. Here we consider semiconductors with four valence electrons like binary compounds from III and V groups of the Periodic Table such as Indium Arsenide. The properties of the aforementioned semiconductors are studied near Brillouin zone center. S and P atomic states create bonding and antibonding molecular orbitals through hybridization. The bonding orbitals are filled by four valence electrons and develop valence band while the antibonding orbitals are empty and form the conduction band shown in Figure 2.1. Considering selection rules, optical transitions from p-like valence band to s-like conduction band are allowed, hence observing strong absorption is expected.

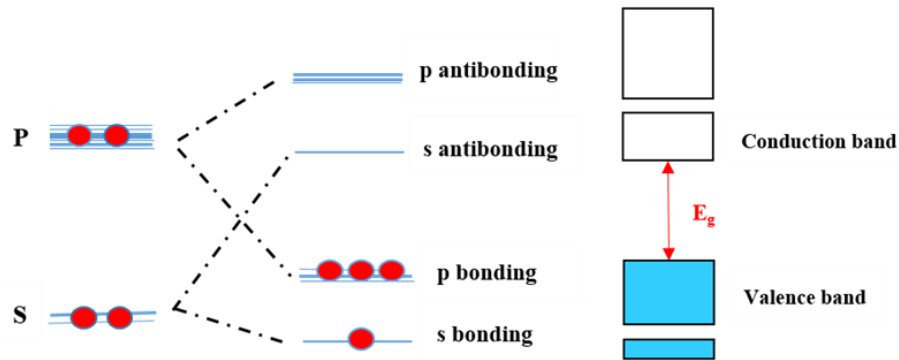


Figure 2.1 Electron levels of materials generated from four valent atoms such as carbon or binary compounds like Indium Arsenide schematics. S and p orbitals turn into bonding and antibonding states by hybridization and induce valence and conduction bands of the crystal.

Band structure of III-V semiconductor compounds such as InAs shown in Figure 2.2. As we see three subbands in the valence band represent the p bonding states while the single conduction band corresponds to s antibonding orbital. The positive curve in the E-k diagram shows the electron band whereas, the three negative parabolas represent hole bands. Two of them are degenerate at $k = 0$ which are called heavy hole and light hole states. The other one is split-off hole band in a lower energy that is a consequence of spin-orbit coupling.

Bandgap is direct here which means that both of the valence band maximum and the conduction band minimum take place at $k = 0$ in the Brillouin zone. There is not a considerable change in wave vector to conserve momentum. Therefore interband absorption is presented by vertical arrows in the E-k diagram. However, in the case of indirect bandgap, minimum of the conduction band occurs at $k \neq 0$. As a result, not only a photon absorption but also, participation of a phonon is required for the transition to conserve momentum.

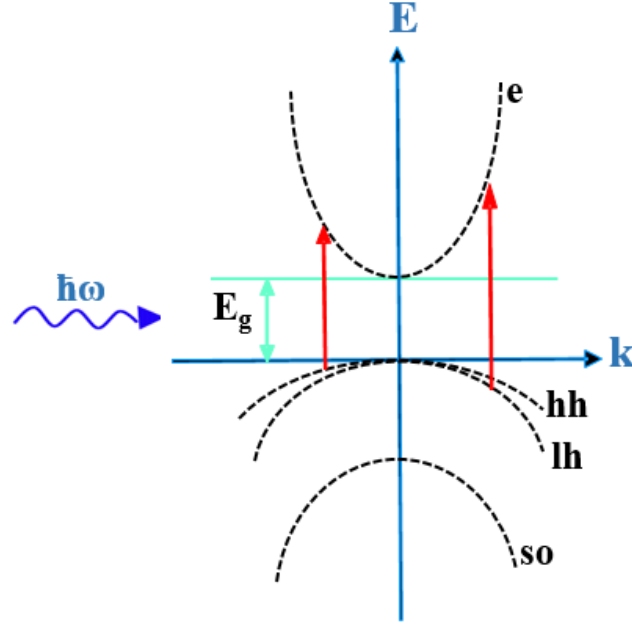


Figure 2.2 Schematic diagram of band structure of direct gap III-V semiconductors near to the center of Brillouin zone.

In quantum wells, electrons and holes are confined in one direction while they can move freely in the other two directions. The wave functions for a quantum well in which electrons and holes have free motion in x-y plane but are confined in z direction are given by:

$$\Psi(x, y, z) = \psi(x, y)\phi(z) \quad 1.1$$

To determine the wave functions and energies of quantized states in z direction we can model that with one dimensional potential well with infinite barriers as a primary case. We consider a quantum well with thickness of L_z in which the potential is zero for $0 < z < L_z$ and infinite elsewhere. The Schrödinger equation inside the well is:

$$\frac{-\hbar^2}{2m^*} \frac{\partial^2 \phi_n(z)}{\partial z^2} = E_n \phi_n(z) \quad 1.2$$

E_n and φ_n are energy and wave function of n th solution of equation above respectively. \hbar is reduced Plank constant and m^* is the effective mass of electrons. The solutions that satisfy boundary condition as $\varphi=0$ at infinitely high barriers are in the form of:

$$\varphi_n(z) = \sqrt{\frac{2}{L_z}} \sin\left(\frac{n\pi}{L_z} z\right) \quad 1.3$$

Quantum confinement in the z direction leads to quantization of energy levels E_n and wave vectors k_z . n is an integer which indicates quantum number of state.

$$E_n = \frac{\hbar^2}{2m^*} \left(\frac{n\pi}{L_z}\right)^2, \quad k_z = \frac{n\pi}{L_z} \quad 1.4$$

Figure 2.3 shows the first three wave function of infinite potential well. Confinement energies are proportional to n^2 in units of $\hbar^2 / 8m^* L_z^2$ where $n=1$ is ground state and higher levels are excited states.

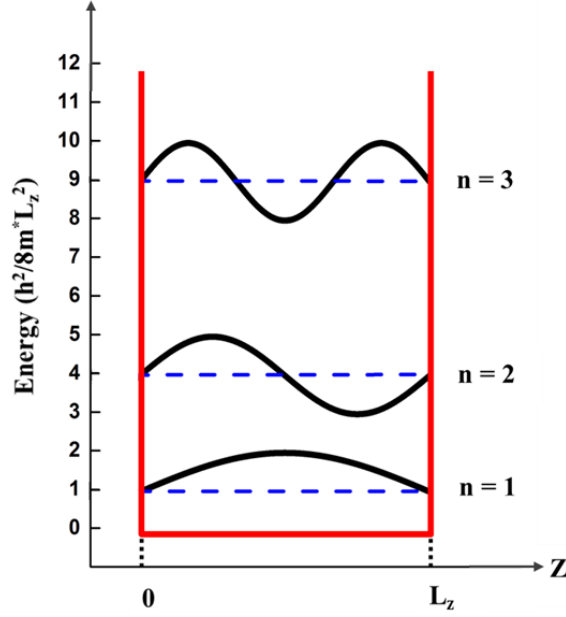


Figure 2.3 First three energy levels and corresponding wave functions of an infinite potential well of width L_z .

2.2 Optical absorption of quantum wells

Here we study linear interband optical absorption of III-V quantum wells ignoring excitonic effects. When the light is radiated in the z direction perpendicular to the well, instead of conservation of momentum, selection rule will be considered because in this direction, energy states are quantized. Electron travels from initial state in the valence band to the final state in the conduction band by absorbing a photon. Absorption rate can be deduced through Fermi's golden rule which is directly dependent to the density of states and squared matrix element. Matrix element includes dipole moment and electron-hole overlap integral [7]. Selection rule for an infinite quantum well indicates that transitions from n th hole band to the n' th electron band is allowed if only $\Delta n = n' - n = 0$. This follows from overlap integral consist of envelope wave functions of electron and hole states. Since we have sinusoidal standing waves for the well, overlap integral is nonzero if $n' = n$.

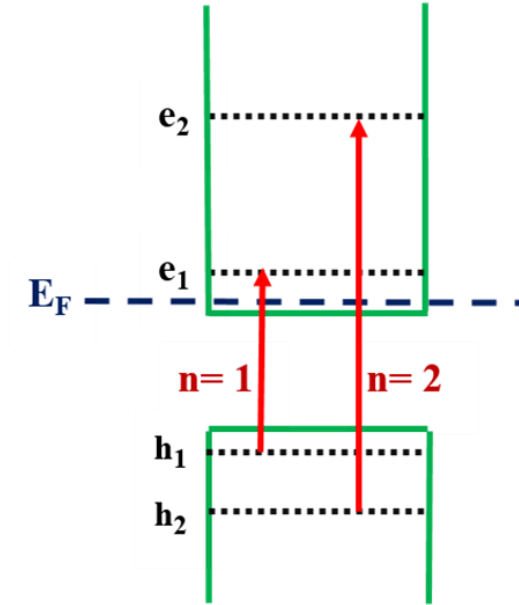


Figure 2.4 The first and second allowed interband optical transitions in accordance with selection rules in a quantum well.

However electrons and holes have discrete energy levels in the quantum well, they can move freely in the x-y plane of the well and have kinetic energy associated with the free motion. Therefore the total energy can be determined by following:

$$E_{total} = \frac{\hbar^2}{2m^*} (k_x^2 + k_y^2 + (\frac{n\pi}{L_z})^2) \quad 1.3$$

Since density of states of the motion in x-y plane is constant, it is stepwise for the discrete confinement energy levels. So the optical absorption of quantum well consists of steps with outset energies follows from quantized energies while each step corresponds to one quantum number.

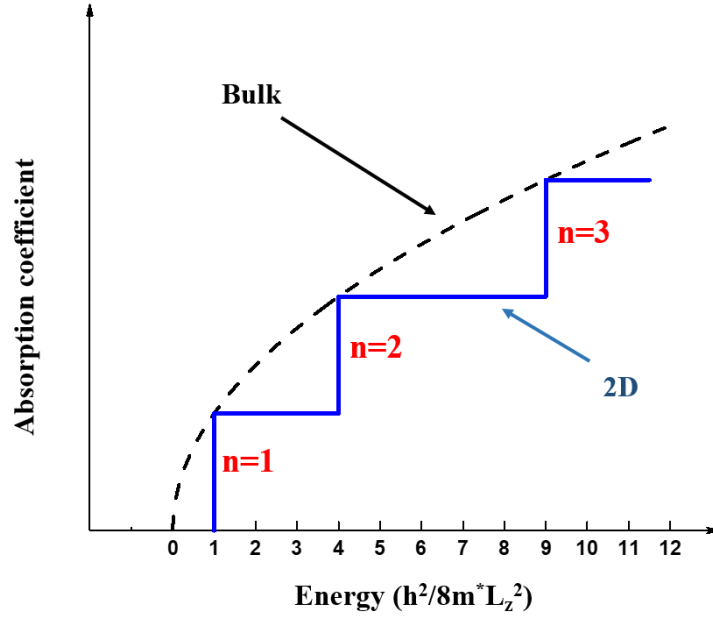


Figure 2.5 The step like absorption coefficient of an infinite quantum well of width L_z compared to the 3D case.

2.3 Quantum Optical absorption of InAs membrane

Optical absorption properties of InAs membranes with thickness $L_z \sim 3-19$ nm on CaF_2 substrate was studied by Fang et al [8]. Since bulk InAs has large Bohr radius, electrons and holes will be confined strongly in sub-20-nm thicknesses. InAs quantum membranes (QMs) sandwiched by air in one side and CaF_2 of large bandgap on the other side behave like infinite potential wells. Therefore allowed interband transitions followed from selection rules are $e_n\text{-}hh_n$ (nth heavy hole subband to nth electron state) transitions and $e_n\text{-}lh_n$ (nth light hole subband to nth electron level) transitions. Fourier transform infrared (FTIR) is used to measure transmission (T), and reflection (R) of InAs QMs at room temperature. T is proportion of incident light transmitted through the membrane while R is the portion of light which is refracted from the membrane. The range of measurement was $2414\text{-}9656\text{ cm}^{-1}$ in which CaF_2

is transparent. Using $A+T+R=1$ relation, optical absorptance (A) that is the portion of light absorbed by the sample has been calculated.

Experimental data shown in Figure 2.6 indicates that absorptance spectra of InAs QMs with different thicknesses are step like and each step's amount is about $1.6 \pm 0.2\%$ resulting from quantized interband transitions.

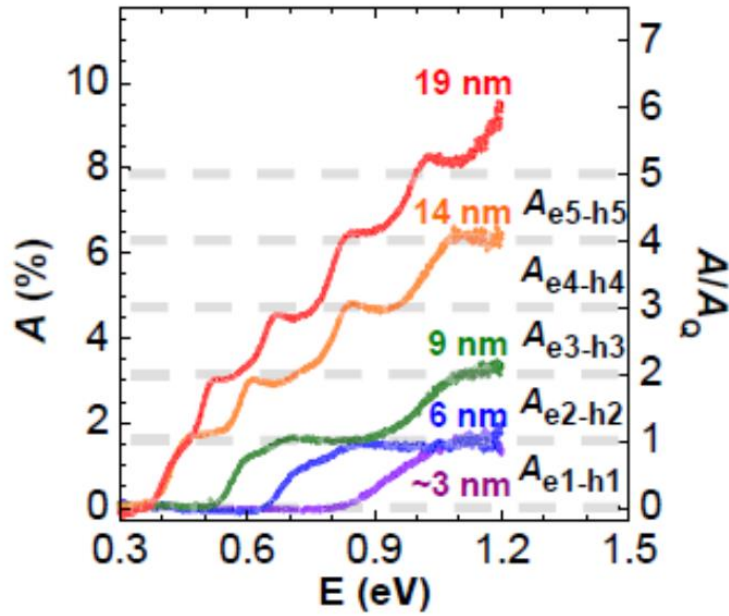


Figure 2.6 Experimental absorption of InAs QMs of different thicknesses at room temperature. The magnitude of quantum absorptance A_Q for each step is 1.6% and are shown by dashed lines. The A_{en-hn} indicates the absorption corresponding to the interband transition from n th hole state to the n th electron state [8].

Using Fermi's golden rule, optical absorption coefficient $\alpha'(\hbar\omega)$ of an infinite potential well with thickness of L_z can be obtained. For the incident electromagnetic wave with polarization vector \hat{e} and frequency ω shined perpendicularly to the well, the absorption coefficient is the following [9],

$$\alpha'(\hbar\omega) = \frac{e^2}{n_r c \epsilon_0 m_0^2 \omega} \frac{\mu}{\hbar^2 L_z} |\hat{e} \cdot \mathbf{p}_{cv}|^2 \quad 1.4$$

Where e is the charge of electron, μ is the reduced electron-hole mass ($1/\mu = 1/m_e + 1/m_h$), n_r is the real part of refractive index, c is the speed of light, ϵ_0 is the vacuum permittivity, m_0 is the rest mass of electron, \hbar is reduced Planck's constant, and $|\hat{e} \cdot \mathbf{p}_{cv}|^2$ is momentum matrix element. On the other hand, k.p perturbation theory results to $1/\mu = 4|p_{cv}/m_0|^2/\hbar\omega$ which leads to cancel $|p_{cv}|^2$ in the numerator. The simplified term left behind all of the cancelations is $\alpha' L_z = \pi(e^2/4\pi\epsilon_0\hbar c)/n_r$ which is the absorption corresponding to each step where $(e^2/4\pi\epsilon_0\hbar c)$ is fine structure constant (α) and it amounts 1/137.

Like graphene, an atomically thin 2D material absorbs $\pi\alpha = 2.3\%$ portion of light [2]. However, the measured absorptance amount for each step (1.6%) is less than $\pi\alpha$ evidently. It means we need a correction since the quantum membranes are not free standing and lied down on a substrate therefore the refractive index of surrounding medium should be taken into account. Considering Fresnel law, the membranes with substrate of refractive index n reflect $(1-n)/(1+n)$ portion of incident electric field E_0 while the transmitted part is $2/(1+n)$. Hence the optical absorption is decreased by $\{2/(1+n)\}^2$ thus the correction factor will be $n_c = \{(1+n)/2\}^2$ which is called the local field correction factor. The quantum absorption will be the following

$$A_Q = \frac{\pi\alpha}{n_c} = \pi\alpha \left(\frac{2}{1+n}\right)^2 \quad 1.5$$

Considering the refractive index of CaF_2 $n = 1.43$, $n_c = 1.48$, the absorption step will be 1.58% which is consistent with experimental results with 3% error.

Chapter 3

Optical Properties of Graphene

After understanding the optics of 2D materials, we study optical properties of graphene. Unique band structure of graphene is the source of its distinct optical properties. Two optical contributions which give rise to optical absorption of graphene are interband and intraband transitions. We can modify the optical transitions in graphene through doping. Broadband optical response of highly doped graphene which is grown by CVD technique and transferred on transparent substrate is investigated afterwards.

3.1 Electronic structure of graphene

The electronic band structure of graphene has been studied theoretically long before its existence [10]. It can be derived using tight binding model. Graphene is formed by carbon atoms in a honeycomb lattice structure [11, 12]. An isolated carbon atom with electronic structure of $1s^2 2s^2 2p^2$ has four electrons in the outer shell called valence electrons which can make new orbitals through hybridization. The result is three sp^2 orbitals from the interaction of s orbital with p_x and p_y leaving a pure p orbital p_z . The hybridized sp^2 orbitals are arranged in the xy-plane with 120° angles by σ bonding to

the three neighboring atoms. Therefore the output is a two dimensional honeycomb lattice with strong σ bonds. The energy gap between bonding and antibonding sigma orbitals is so large that electrons cannot participate in electrical conductivity of graphene. However the p_z orbitals perpendicular to the plane give rise to the conductivity of graphene through π bonding and π^* antibonding.

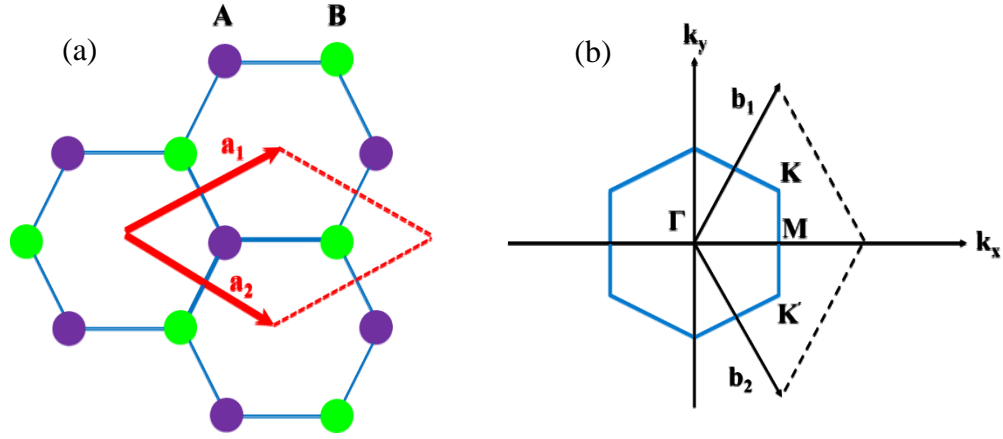


Figure 3.1 schematic of lattice structure of graphene (a) Honeycomb crystal structure of graphene with a unit cell consisting of two carbon atoms. (b) The first Brillouin zone of graphene with hexagonal shape where all corners of the hexagon are Dirac points. The unit cell of graphene includes two inequivalent atoms with primitive lattice vectors \mathbf{a}_1 and \mathbf{a}_2 as shown in the Figure 3.1(a).

$$\mathbf{r}_{\mathbf{a}_1} = \frac{a}{2}(3, \sqrt{3}) \quad \mathbf{r}_{\mathbf{a}_2} = \frac{a}{2}(3, -\sqrt{3}) \quad 3.1$$

Where $a = 2.46 \text{ \AA}$ is the lattice constant. The first Brillouin zone shown in Figure 3.1(b) yields from planes bisecting reciprocal base vectors \mathbf{b}_1 and \mathbf{b}_2 which forms the same hexagon of real space lattice rotated by 90 degrees.

$$\mathbf{r}_{b_1} = \frac{2\pi}{3a}(1, \sqrt{3}) \quad \mathbf{r}_{b_2} = \frac{2\pi}{3a}(1, -\sqrt{3}) \quad 3.2$$

The six corners of the first Brillouin zone are two inequivalent group labelled K and K' which are called Dirac points. Moving from K to K', there is the saddle-point singularity at M point. The center of Brillouin zone is Γ .

$$\mathbf{K} = \frac{2\pi}{3a}\left(1, \frac{1}{\sqrt{3}}\right) \quad \mathbf{K}' = \frac{2\pi}{3a}\left(1, -\frac{1}{\sqrt{3}}\right) \quad 3.3$$

The dispersion relation of electronic bands in the nearest neighbor approximation of graphene has the form

$$E_{\pm}(k) = \pm \gamma_0 \sqrt{1 + 4 \cos\left(\frac{\sqrt{3}k_x a}{2}\right) \cos\left(\frac{k_y a}{2}\right) + 4 \cos^2\left(\frac{k_y a}{2}\right)} \quad 3.4$$

Where γ_0 is the nearest neighboring hopping energy [13, 14]. k_x and k_y are x and y components of momentum. By plotting energy as a function of k according to equation (3.4), two curves will be obtained from which, the upper one is denoted by π^* band and the lower one is called π band. The two bands are degenerate at Dirac points. Dirac point is also the Fermi energy level E_F in intrinsic graphene. There are two atoms in unit cell of Brillouin zone therefore their two electrons will fill the π band and leave the π^* band empty. The filled π band noted as valence band and the empty conduction band (π^* band) resemble semiconductor structure with a major difference that in graphene the bandgap is zero. Since the Fermi energy corresponds to $E_{\pm}(k) = 0$ at Dirac point, by expanding equation (3.4) around Fermi level we acquire the linear dispersion relation.

$$E_k = \pm \hbar v_f |\mathbf{k}| \quad 3.5$$

Where $V_f = \sqrt{3}\gamma_0 a / 2\hbar \approx 10^6$ m/s is the Fermi velocity of Dirac fermions. It can be deduced from equation (3.5) that electrons in graphene behave as massless particles considering the effective mass as derivation of energy with respect to k .

3.2 Doping of graphene

Doping can modulate electrical and optical properties of graphene effectively. There are different methods to dope graphene in order to tune its charge carrier's concentration. Electrical gating such as back-gating, top-gating or electrolyte gating can dope graphene by applying the gate voltage. However, chemical doping including substitutional doping and surface transfer doping controls charge carrier density of graphene by exploiting chemical species. In this study, we used electrolyte gating and surface transfer doping techniques. Electrolyte gating is applied in this chapter while surface transfer chemical will be considered in chapter 4.

Electrolyte gating is an electrostatic doping method applied for optoelectronic devices. This is done on supercapacitors with electrolyte between graphene and a metal electrode. The electrolyte liquid carries mobile ions which get polarized by applying a voltage. As a result, a few nanometer-thick electrical double layer (EDL) are generated at the graphene and metal electrode's surfaces shown in Figure 3.2.

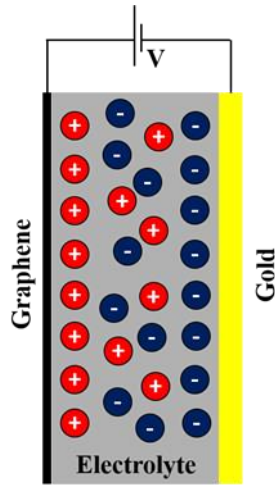


Figure 3.2 Electrolyte gating method of graphene. Applied gate voltage generates an electrostatic potential difference between the gold electrode and the graphene. Fermi energy is shifting by increasing charge carriers through electric field.

The charged ions of EDL induce electric fields which change the carrier density up to 10^{14} cm^{-2} corresponding to about 1 eV Fermi energy. The drawback of this method is electrochemical window of the electrolyte to obtain high charge carrier density on graphene. Narrow electrochemical window of electrolyte can restrain concentration of charge carriers and shifting Fermi energy of graphene. Here we used the ionic liquid which has a wide electrochemical window enabling us to shift Fermi energy of graphene to a greater extent than 1eV.

When electrons are added to the conduction band of graphene, it is called n-doped, while addition of holes to the valence band of graphene leads to p-doped graphene [15].

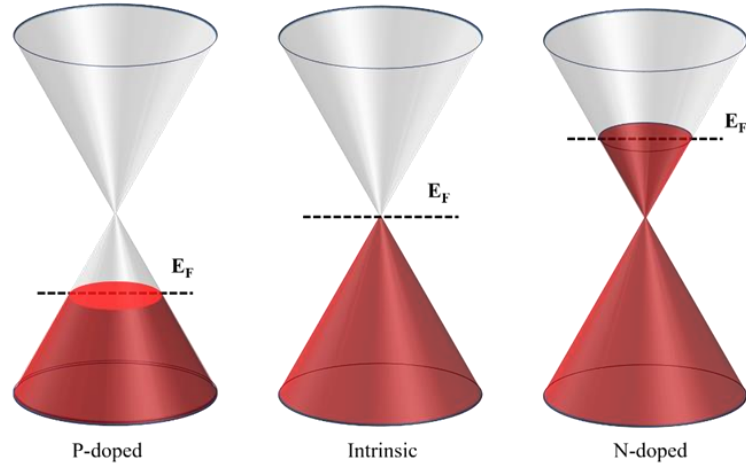


Figure 3.3 Graphene's Dirac cones in three different cases. P-doped graphene is obtained by introducing holes to the graphene and therefore, Fermi energy shifted down. In the pristine graphene, Fermi level is at the Dirac point. The n-doped graphene is electron injected and Fermi energy is shifted up.

3.3 Optical properties of graphene

Strong interaction of light with graphene extends over wide range of frequencies from UV and visible to far infrared and terahertz regions [16-18]. Two different types of optical transitions induce optical absorption of graphene. For high energy photons, optical absorption of graphene is dominated by interband transitions which is frequency independent and has a constant universal amount $\pi\alpha \approx 2.3\%$. This transition appears in visible and near infrared ranges. However intraband transitions

dominate at low energy photon ranges such as far infrared and terahertz that electrons can only move within bands.

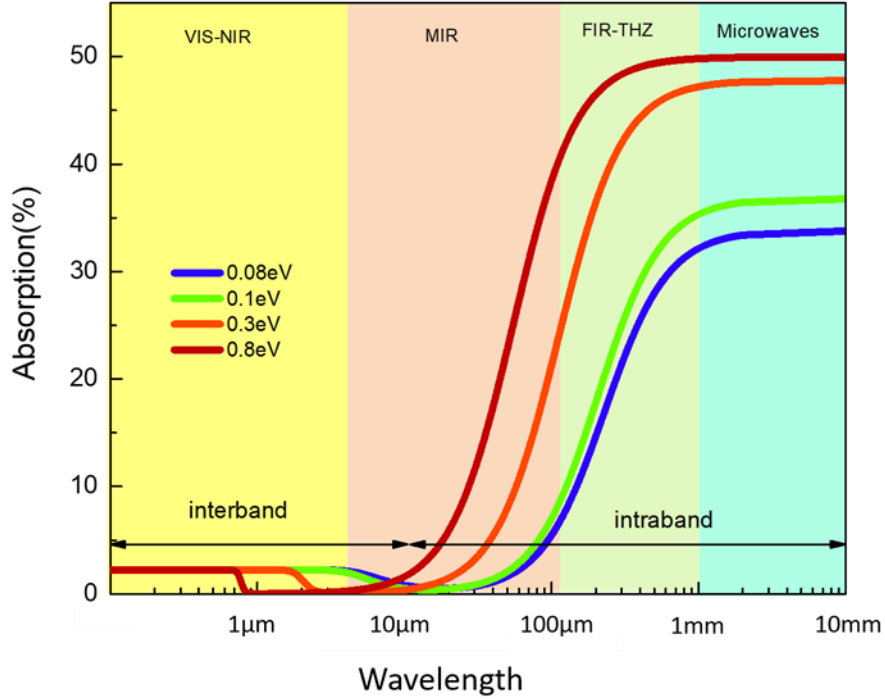


Figure 3.4 Wide-range optical response of graphene illustrated from visible to microwave spectrum. Graphene absorbs 2.3% of light at visible-near infrared region in which interband transitions arise from high energy photons. However, the absorption reaches 50% due to intraband transitions for low energy photons at terahertz and microwave area.

Both of these optical contributions depend totally on fermi energy of graphene. During the doping process, Fermi energy is shifted and consequently the cut-off frequency of interband transitions shifts to higher energies; however, the amount of absorption remains constant. Even so, in the intraband contributions, the high level of doping increases the number of free carriers and enhances the absorption. Figure 3.4 presents the modelling of optical absorption of monolayer graphene and its

broadband response to electromagnetic waves. Optical absorption of graphene can be tuned by shifting Fermi energy through electrostatic gating or chemical doping.

3.3.1 Interband optical transitions

The incident light to the graphene can excite electrons to travel from valence band to conduction band leaving holes illustrated in Figure 3.5(a). These transitions are called interband transitions and they take place when a photon has enough energy to provide for the band to band transition of an electron. The photon energy should be at least twice the Fermi energy of graphene with respect to cone tip to be capable of creating electron-hole pair.

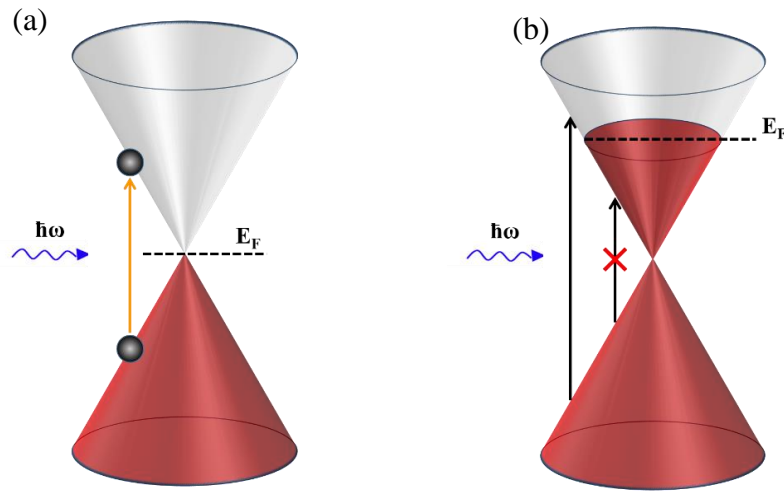


Figure 3.5 Interband transitions. (a) A photon with energy of $2E_F$ or more is absorbed by an electron exciting it from valence band to conduction band. (b) Optical transitions for energies less than $2E_F$ are blocked.

When graphene gets doped, the Fermi energy is shifted. Due to Pauli Exclusion Principle, interband optical transitions are not allowed at energies below $2E_F$, shown in Figure 3.5(b). Therefore it is called Pauli blocking. In the Pauli blocking region, photons with energy less than $2E_F$ cannot excite electrons, therefore, banned optical transitions lead to vanishing the optical conductivity of graphene.

Graphene's remarkable properties rest on its optical conductivity derived from Kubo formalism [19]. The graphene conductivity consists of interband and intraband conductivities which are complex functions. The real part of interband conductivity for the graphene with Fermi energy of E_F at temperature T is frequency dependent as following:

$$\text{Re } \sigma_{\text{inter}} = \frac{\sigma_0}{2} \left\{ \tanh\left(\frac{\hbar\omega + 2E_F}{4k_B T}\right) + \tanh\left(\frac{\hbar\omega - 2E_F}{4k_B T}\right) \right\} \quad 3.6$$

Where ω is the angular frequency of the incident photon, \hbar is the reduced Planck's constant, k_B is the Boltzmann constant and $\sigma_0 = e^2 / 4\hbar$ [2] is the universal conductance of graphene. The imaginary part of interband conductivity is frequency dependent as well and is expressed as:

$$\text{Im } \sigma_{\text{inter}} = \frac{\sigma_0}{2\pi} \ln \left\{ \frac{(\hbar\omega + 2E_F)^2}{(\hbar\omega - 2E_F)^2 + (2k_B T)^2} \right\} \quad 3.7$$

The complex interband conductivity of graphene for different temperatures is shown in Figure 3.6. The stepwise part of the plot illustrates the real interband conductivity which demonstrates the interband optical absorption while the other one presents the imaginary part of the conductivity [20].

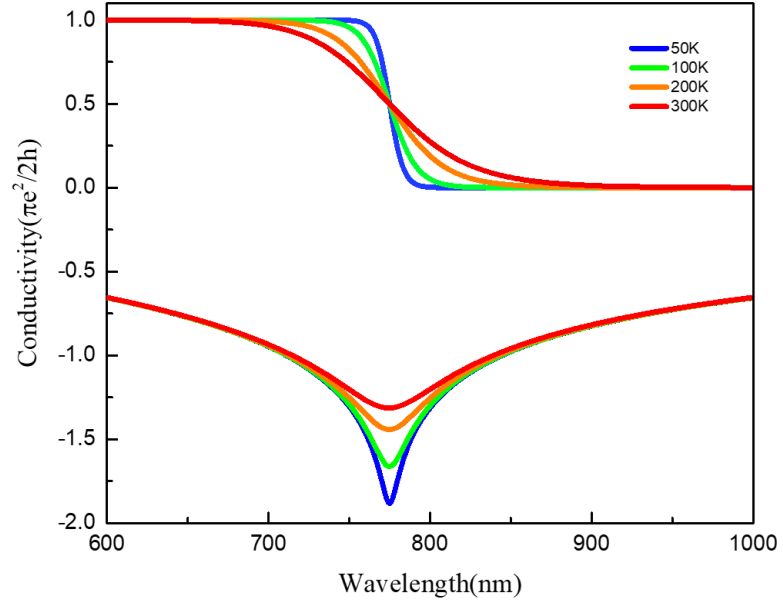


Figure 3.6 Modeled real and imaginary parts of conductivity of graphene at different temperatures. Both parts are temperature dependent.

The stepwise optical absorption of graphene shown in Figure 3.7 (b) is calculated at different Fermi energies. This behavior comes from the real part of optical conductivity. $A(\omega) = (4\pi/c)\text{Re}\sigma(\omega) = \pi\alpha$ shows the relation between interband optical conductivity and absorption. $T = (1 + \pi\alpha/2)^{-2} \approx 1 - \pi\alpha = 97.7\%$ gives the transmittance of graphene in the visible region [21]. As the reflection of graphene in this range is negligible, the optical absorbance of graphene will be $A = 1 - T \approx 2.3\%$.

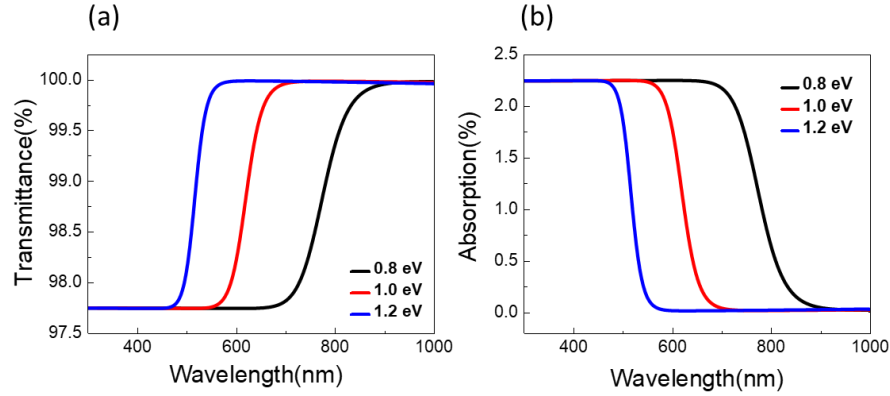


Figure 3.7 Optical spectrum of graphene at different Fermi energies in visible range. (a) Transmittance of graphene is about 97.7% in visible range (b) absorption spectrum of graphene is about 2.3% for energy photons of $2E_F$. Therefore, by increasing Fermi energy, transition of photons with less energy is blocked.

The optical spectrum of graphene in visible range indicates the constant absorption of 2.3%. When Fermi energy of graphene shifts through doping, optical transitions for energies below $2E_F$ are blocked and absorption goes to zero in that frequency range as shown in Figure 3.7.

3.3.2 Intraband electronic transitions

The optical response of graphene in far infrared and terahertz ranges in which, photons have low energies, is mainly controlled by intraband transitions. The optical absorption in this area, is noticeable and is contained by free carrier response. When photons excite carriers between the levels inside the valence or conduction band, intraband transitions take place. For instance, absorption of photons can excite electrons from an occupied level under the Fermi level to an empty state over E_F . To conserve energy and momentum, the process should include either phonon scattering or defect scattering as an intermediate state.

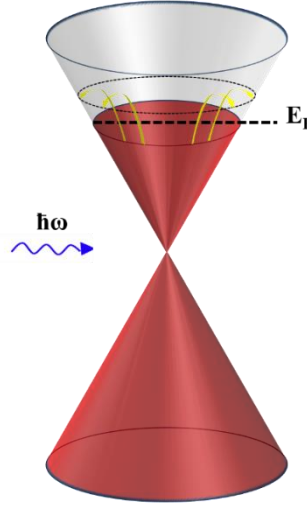


Figure 3.8 Low energy photons in the conduction band can excite electrons within the band called intraband transition.

When the density of free electrons in the conduction band is increased, the intraband carrier transition increases which is followed by a dramatic increase in the absorption shown in Figure 3.8. This holds true also for the excess density of free holes in the valence band. The free carrier optical absorption of graphene can be described by Drude model in which, the excited electrons collide with phonons and impurities and get scattered afterwards. The frequency dependent conductivity with the electron scattering time τ is as the following [22, 23],

$$\sigma(\omega) = \frac{\sigma_{dc}}{1 + i\omega\tau} \quad 3.8$$

Where $\sigma_{dc} = e^2 E_F \tau / \pi \hbar^2$ the dc conductivity [5], ω is the angular frequency of light and e is the charge of electron. The separated real and imaginary parts of intraband conductivity are:

$$\text{Re } \sigma(\omega) = \frac{\sigma_{dc}}{1 + \omega^2 \tau^2} \quad , \quad \text{Im } \sigma(\omega) = \frac{\sigma_{dc} \omega \tau}{1 + \omega^2 \tau^2} \quad 3.8$$

The diagram of equations above is shown in Figure 3.9 (a) and 3.9(b) for different quantities of Fermi level.

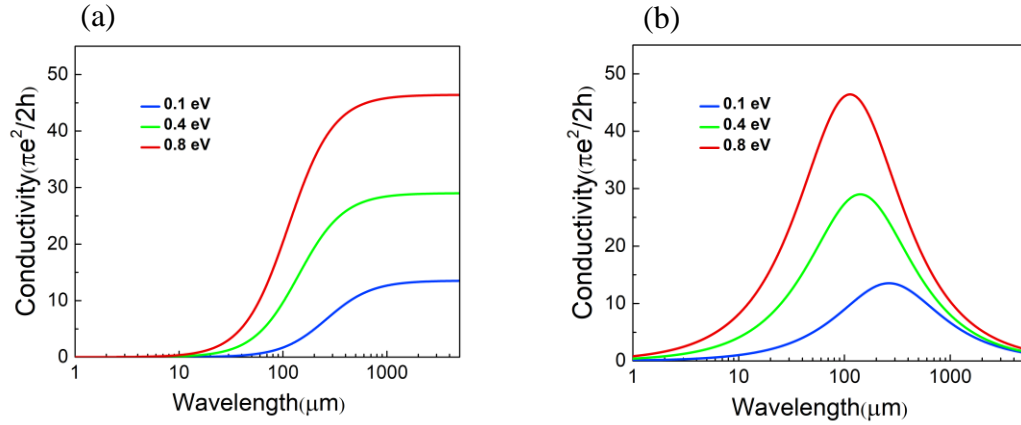


Figure 3.9 Intraband conductivity (a) Real part of Drude conductivity at different Fermi energies. (b) Imaginary Drude conductivity of different Fermi energies.

3.4 Synthesis of graphene

Graphene was first fabricated from bulk graphite using scotch tape by mechanical exfoliation [15]. This method provides graphene with high carrier mobility but the large area graphene cannot be obtained. There are other methods such as growing graphene on SiC substrates by epitaxy, annealing solid carbon sources and chemical vapor deposition (CVD). During CVD technique, the gas-phase precursors accumulated on the surface react and lead to the deposition of a thin layer following from chemical reactions in high temperature and low pressure. In the case of graphene, CVD method is the promising way to produce large area graphene in a low

cost [24]. Carrier mobility of CVD graphene is lower compared to graphene yielded from exfoliation method [25], however, it can be improved by optimization [26]. CVD method can be applied to grow both monolayer and multilayer graphene. For the single layer growth of graphene, we use copper substrate since it is an effective catalyst to transform hydrocarbons into graphene and its carbon solubility is negligible even in high temperature therefore it is more likely to have a monolayer coverage of graphene on copper's surface.

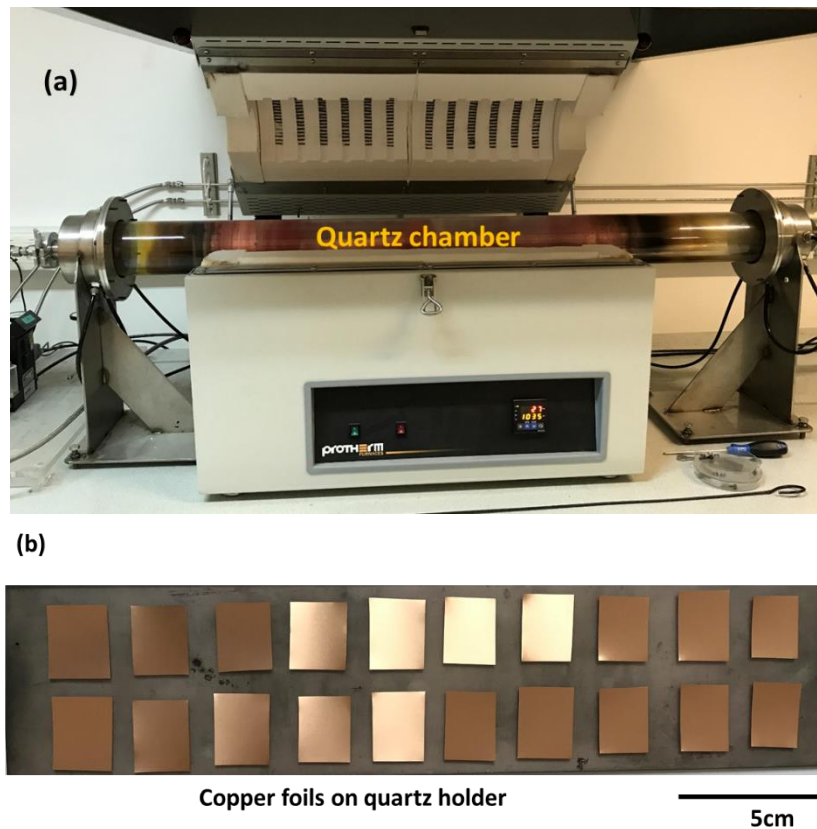


Figure 3.10 (a) Quartz chamber is placed in the furnace and the temperature of furnace can rise up to 1070 degrees. (b) Cu foils are cut and arranged on the holder.

The CVD system used in our lab, consists of a quartz chamber settled in a furnace including gas sources, a mechanical pump to vacuum the chamber and units to control gas flow.

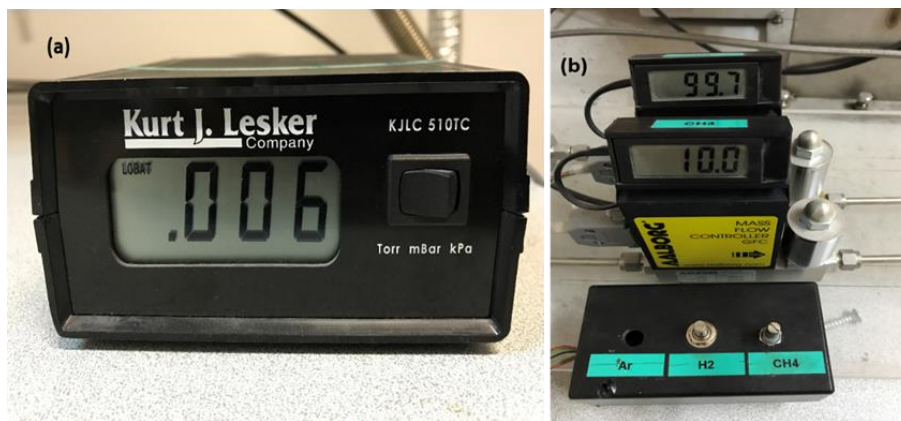


Figure 3.11 (a) Vacuum Gauge showing that chamber is pumped down to a vacuum of 6 mTorr. (b) Mass flow controllers showing flow amount of hydrogen and methane.

As substrates, the ultra-smooth copper foils of thickness $20\text{ }\mu\text{m}$ were cut in $1 \times 2.5\text{ cm}^2$ sizes and put on the quartz holder of size $7 \times 30\text{ cm}^2$ and placed in the chamber. The chamber was then evacuated to 6 mTorr shown in Figure 3.11(a). Then copper substrates were heated under hydrogen H_2 flow with rate of 100 sccm until the temperature reached $1035\text{ }^\circ\text{C}$. It is applied to remove the oxide layer and other chemical residues from the surface of the copper substrates. When the chamber reached $1035\text{ }^\circ\text{C}$, the growth of graphene was initiated by flowing methane CH_4 at a rate of 10 sccm for one minute shown in Figure 3.11(b). During the deposition, a chiller cooled down the edges of the system to avoid damage to the gasket materials. After closing methane flow, the system was cooled down to the room temperature under hydrogen flow. Then the chamber was opened to air to unmount the samples.

3.5 Transfer procedure

The CVD graphene is advantageous since it can be transferred to different sorts of surfaces depending on device type and the desired application area. We transferred graphene onto solid substrates such as glass and quartz and flexible surfaces such as PVC and polyethylene.

To transfer graphene to one of the aforementioned substrates, firstly the graphene on ultra-smooth copper foil with 20 μm thickness was covered by photoresist (Shipley 1813) shown in Figure 3.12(a). The samples were put in the oven 60 $^{\circ}\text{C}$ and baked for 24 hours. Afterwards, the copper was dissolved using wet etching. For this purpose, Iron chloride (FeCl_3) was used as the copper removing solution. This solution leaves chemical residues on graphene which are difficult to clean. Therefore, a solution of Nitric acid, Hydrogen peroxide, Hydrochloric acid and water was used as copper etchant. The consequent graphene had higher quality and was less contaminated, although, the resultant graphene got chemically doped by Nitric acid. As the last step of the process, the graphene on photoresist was placed on the substrate with graphene facing the surface of substrate. Figure 3.12(c) Illustrates the sample of graphene on photoresist put on polyethylene which placed on a hotplate. The sample was heated up to 90 $^{\circ}\text{C}$ to let the graphene layer stick to the substrate. Then the photoresist was removed by acetone. Then the substrates were further cleaned by isopropyl alcohol (IPA). Graphene on polyethylene is shown in Figure 3.12(d).

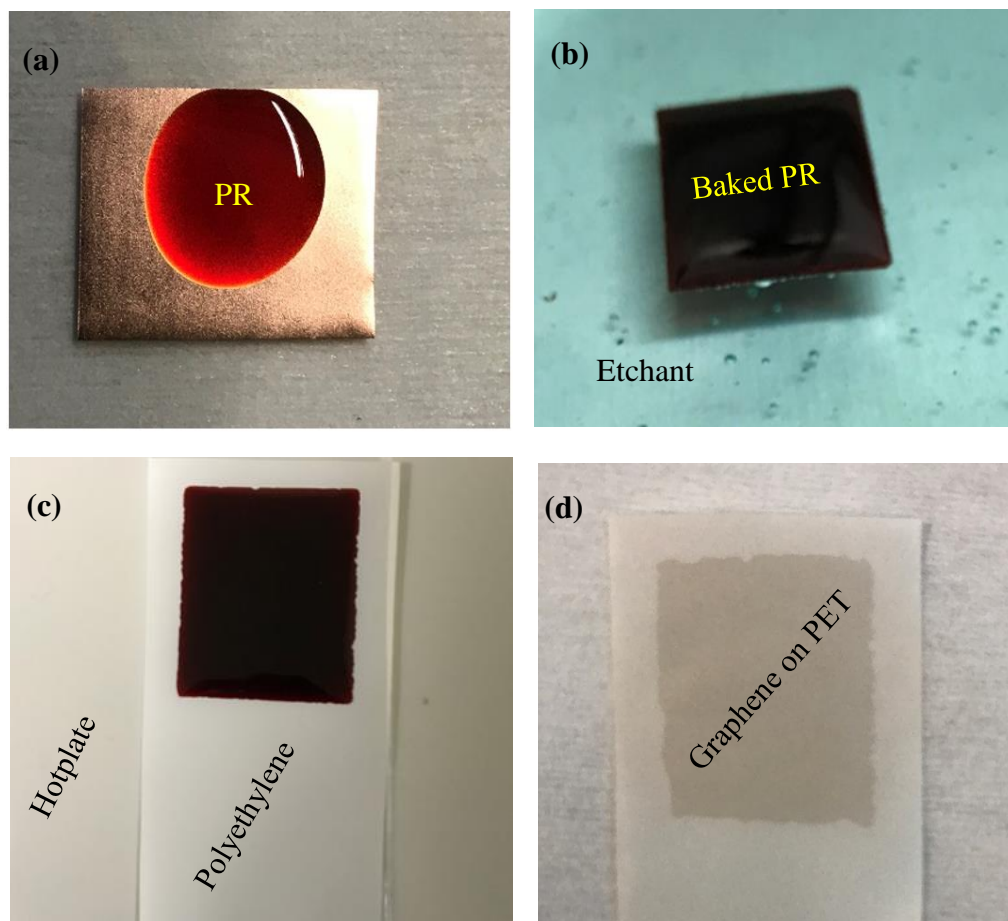


Figure 3.12 Graphene transfer process. (a) Photoresist (PR) on CVD-deposited graphene on Cu. (b) The baked sample in the etchant to remove Cu. (c) Graphene on PR placed on the polyethylene substrate and heated on a hotplate. (d) Graphene on polyethylene where the PR is removed by acetone.

Lamination is another method that we used to transfer graphene. This technique is advantageous for large area graphene. Although we are limited by the size of chamber and holder, there are optimized cylindrical holders through which, graphene samples of the size $30 \times 30 \text{ cm}^2$ can be obtained. The first step of lamination method is to place on-copper foil-deposited graphene onto the substrates such as polyethylene or PVC

(polyvinyl chloride) where the graphene faces PVC. The sample with is protected on both sides by laminated paper using laminating machine. Then as we mentioned before, the copper was etched by solvent. Shown in Figure 3.13(b), we applied tapes at the edges of the sample to create copper stripes as electrical contacts.

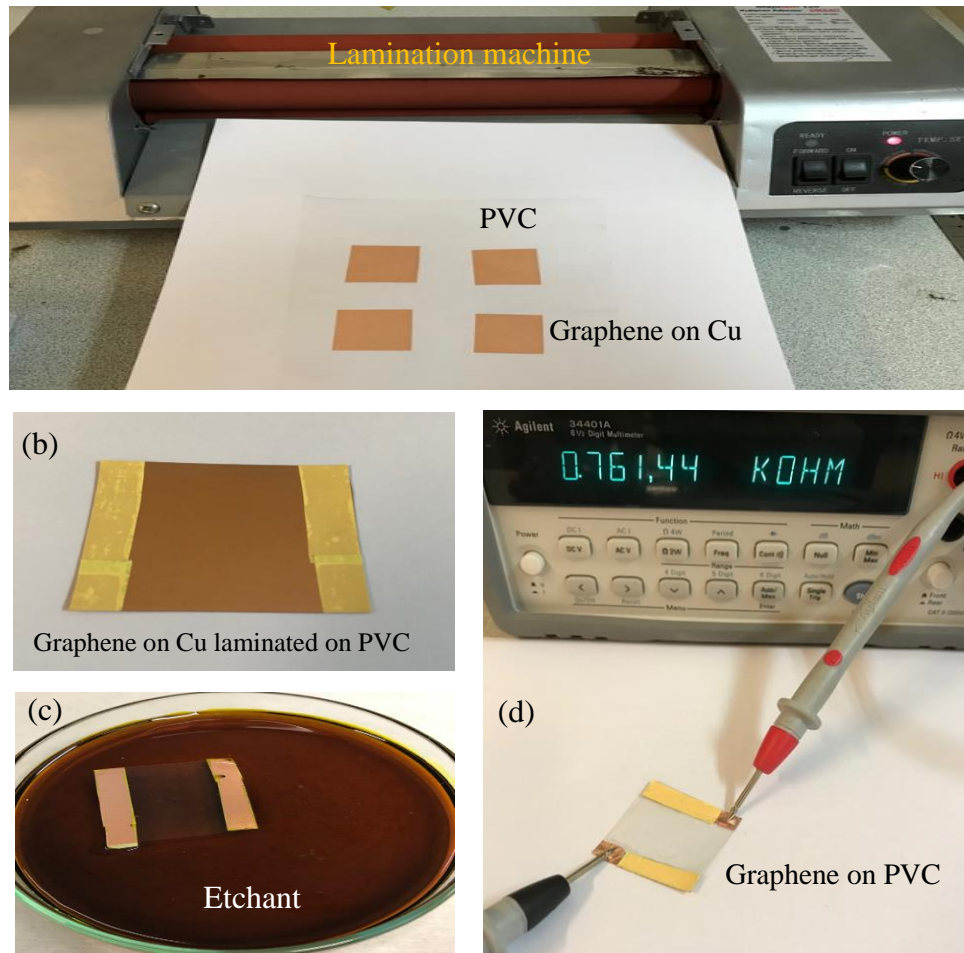


Figure 3.13 Graphene transferred on PVC by lamination. (a) Lamination machine used to laminate CVD graphene on the PVC substrate. (b) Laminated graphene where graphene is between the PVC and Cu. (c) Cu removed by iron chloride to leave graphene on PVC. The tapes used to avoid Cu etching on the sides to take contact from graphene. (d) The conductance of graphene on PVC in kilo ohm.

3.6 Optical response of highly doped graphene

Pristine graphene has frequency independent conductivity of $\sigma_0 = e^2 / 4h$ which gives rise to the frequency independent transmittance that is formulated as

$$T = (1 + \frac{\pi\alpha}{2})^{-2} \approx 1 - \pi\alpha = 0.977 \quad 3.10$$

Where α is the fine structure constant [12, 18, 27]. Nevertheless, the optical response of graphene is highly frequency dependent at low photon energies since it is controlled by free-carrier absorption. Drude conductivity model can explain optical response of graphene in far-infrared region. The sheet conductivity is in the form of

$$\sigma(\omega) = \frac{\sigma_{dc}}{1 + i\omega\tau} \quad 3.11$$

Where, σ_{dc} is the dc conductivity and τ is the scattering time of electron. Drude weight $D = \pi\sigma_{dc} / \tau$ can express the Drude conductivity for microscopic factors. Drude weight has the form of $D = e^2 v_F \sqrt{\pi n}$ for graphene where, v_F is the Fermi velocity of 10^6 m/s and n is the concentration of charge carriers [22, 28].

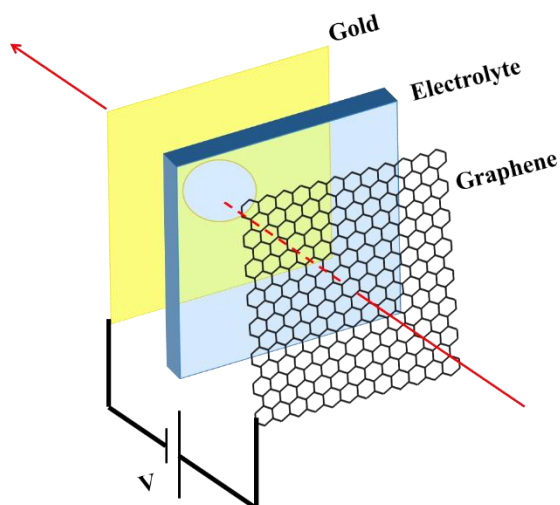


Figure 3.14 schematic of device structure. The device is composed of gold electrode, graphene on a substrate and ionic liquid in between as a gating medium. By applying voltage, ionic liquid gets polarized generating ELD and induce electric field.

An effective device structure of a supercapacitor enabled us to investigate and manipulate optical properties of graphene [29, 30, 31]. We fabricated a capacitor that is composed of graphene and gold electrode with a layer of electrolyte in between shown in Figure 3.14. A monolayer graphene was deposited on copper and transferred onto porous polyethylene with the thickness of 20 μ m. Gold electrode was fabricated by evaporating 60nm thick gold on a PVC substrate. Then a circular window with 6mm diameter was opened as the optical window for the incident beam. Porous polyethylene is transparent in far infrared region. The porosity of polyethylene makes electrolyte hold on to it. Polyethylene with absorbed electrolyte is also transparent up to visible range.

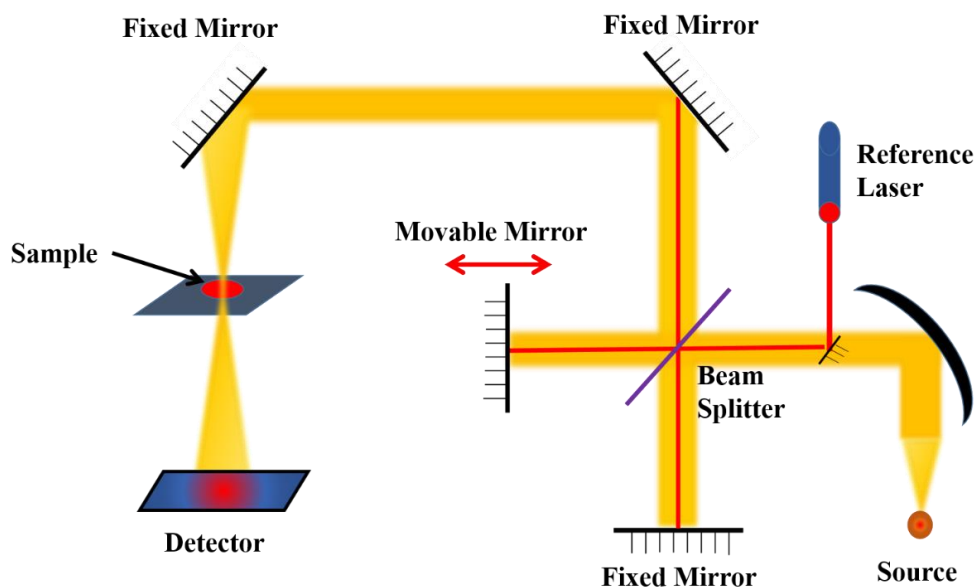


Figure 3.15 The FTIR spectrometer setup

The light radiated from the source goes through the beam splitter and is splitted into two beams one of which, is reflected to the fixed mirror and the other is transmitted to the movable mirror. The moving mirror changes the total path length compared to the fixed mirror. Then the two beams bounce back from the fixed and movable mirror back to the beam splitter and recombine. Since the length paths are varied, they generate constructive and destructive interferences that is called interferogram. The beam goes through the sample and all the wavelength characteristics of the sample's spectrum get absorbed thus these wavelength are deducted from the interferogram. Therefore, energy difference during time for all the wavelengths is determined by the detector. The resultant interferogram is translated by Fourier transform algorithm. Since time and frequency are reciprocal, Fourier function gives the intensity versus frequency instead of time.

Bruker's V70x Fourier-Transform Infrared spectroscopy system used in this study which has a wide range source and corresponding detectors. To measure the spectrum (transmission, absorption or reflection) of a given device, we place it in the

compartment. The charge neutrality point was taken as the gate voltage reference where the dc conductivity is minimum and charge density is zero.

In order to find the reference, first the capacitance and resistance of the device was measured. Using this approach, the charge neutrality point (V_{CN}) or Dirac point is probed by finding the point at which, the capacitance value is the lowest and resistance is the highest. Dirac point is dynamic and can change by different gating configurations. If the graphene is grounded while applying positive voltage to the gold, electrons are generated on the surface of the graphene. In this configuration, if the applied voltage is scanned from the Dirac point (1 V here) through negative voltages, holes are induced on graphene (hole-doped device) while in the case of positive voltages, electrons would be generated (electron-doped device).

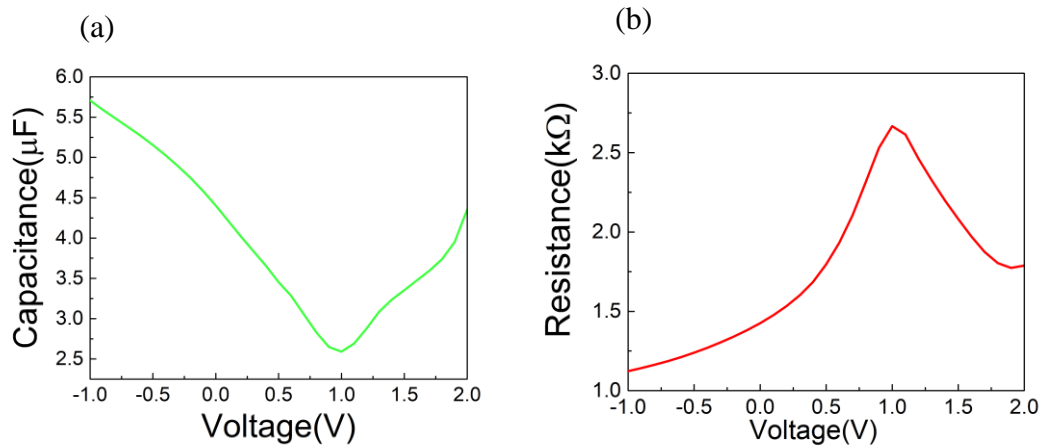


Figure 3.16 To Find the Charge neutrality point (a) Capacitance and (b) Resistance of graphene device vs gate voltage is measured.

The Fermi energy of graphene for different gate voltages can be extracted from the visible and NIR cut-off wavelengths. In this regard, the transmission of the devices were measured in the visible and NIR ranges for both the electron and hole doping regimes.

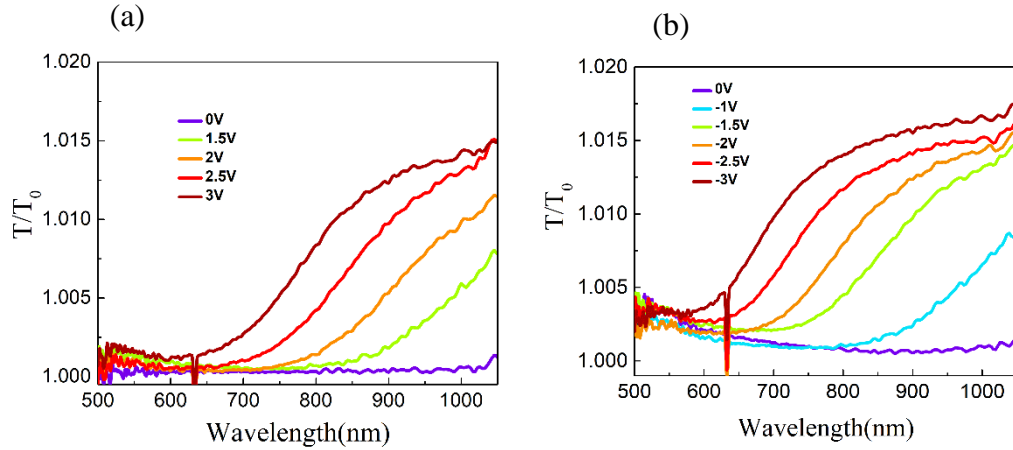


Figure 3.17 Normalized transmittance of graphene device at visible for (a)electron doping regime and (b)hole doping regime of different Fermi energies.

The absorption of free standing graphene is 2.3% in the visible through NIR ranges, although it decreases for graphene on dielectric substrate if the refractive index of the substrate is taken into account. The polyethylene with ionic liquid is transparent at visible range with a refractive index of about 1.6. Therefore, the absorption is calculated to be about 1.4% using equation 2.5. Since reflection in this range is negligible, transmittance is nearly equal to absorption subtracted from unity. This is almost in agreement with the experimental measurements in Figure 3.17 where absorption is 1.5%.

Fermi energy of graphene can be extracted at different gate voltages using Pauli blocking principle. At high energy photons, electrons absorb enough energy to excite from valence band to conduction band leaving holes. When Fermi energy is shifted to higher energies, the transitions for photons with energies less than $2E_F$ energy barrier, are blocked. $2E_F$ at each gate voltage equals to the corresponding cutoff wavelength.

Figure 3.18 represents the calculate Fermi energies at visible range using spectrum of Figure 3.17 for both hole and electron doping.

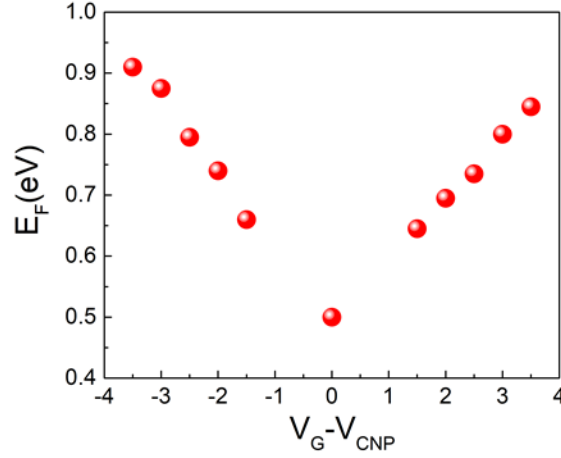


Figure 3.18 Extracted Fermi energies of different gate voltages from cutoff wavelength.

Transmittance spectrum of graphene device at NIR-MIR range shown in Figure 3.19 is only measured for electron doping regime.

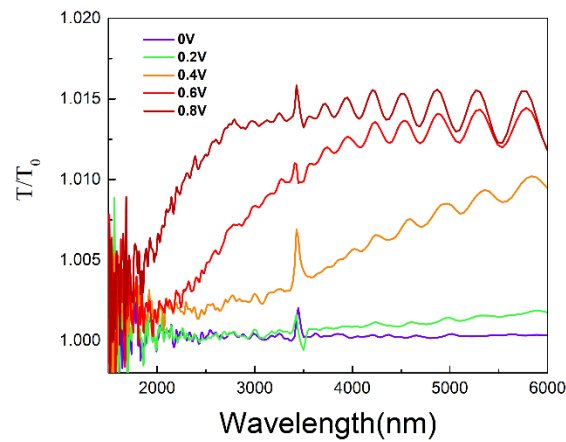


Figure 3.19 Differential transmittance of graphene device at near and mid infrared for electron doping regime.

The oscillations in the transmission spectrum is due to multiple reflection between graphene and gold surfaces. Portion of light transmitted from graphene layer reaches the gold electrode which results in multiple short beams that interfere with each other. It leads to the multiple transmission which is indicated as oscillations in the transmission spectrum.

FTIR spectrometer can measure optical response of graphene at low frequencies using far infrared source and wide range detector which can go down to 50cm^{-1} wavenumber or 1.5 terahertz.

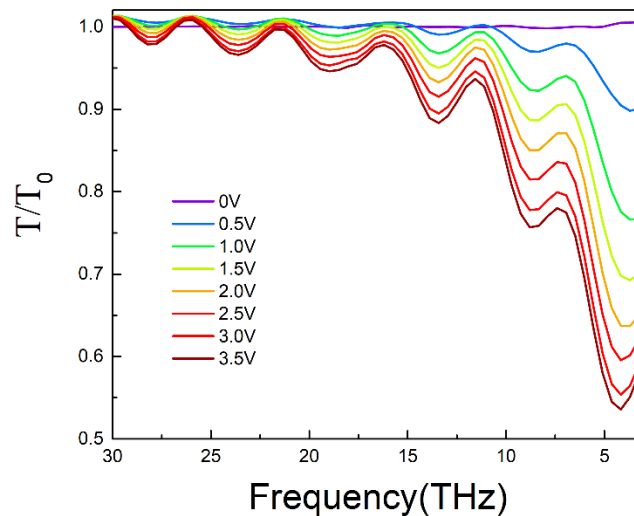


Figure 3.20 Terahertz transmittance spectrum of graphene device at electron doping regime.

At this range, the optical response of graphene is controlled by free carriers. Low energy photons simulate hot carriers within the band thus, increasing the concentration of free carriers through doping enhances intraband transitions therefore optical absorption intensifies. The suppression of transmittance in Figure 3.20 indicates the dramatic raise of absorption in this range.

Chapter 4

Optical residual absorption of graphene

4.1 Introduction

The electronic band structure of graphene indicates that interband excitations of electrons for energy states below $2E_F$ are banned. Due to Pauli's exclusion principle, only photons with energies higher than $2E_F$ can excite electrons and create electron-hole pairs. Therefore the optical absorption of graphene is expected to drop to zero for energies below the $2E_F$ threshold. However, a considerable absorption below $2E_F$ has been reported [6]. The optical absorption measured in Pauli-blocked region is called optical residual absorption. The residual absorption may follow from both internal and external effects. Charged impurities and structural defects such as vacancies, wrinkles and cracks are the external causes which can lead to residual absorption. In a theoretical study, the effects of charged impurities and unitary scatters (vacancies, cracks, edge defects, etc.) on the infrared optical response of graphene has been examined and a considerable amount of optical conductivity in the

energy region below $2E_F$ was found [32, 33]. Reference (32) indicated that disorders extend energy levels and increase density of states at Dirac point which means that the Pauli exclusion cannot block transitions efficiently and even for energies below $2E_F$, there are still some transitions. The internal source of the residual absorption is explained in terms of many-body interactions like electron-electron, electron-phonon and electron-hole interactions. For instance, e-e and e-ph interactions increase the scattering rate of charge dynamics of graphene in infrared region. The frequency dependent scattering rate gives rise to an increase in the optical conductivity in comparison with Drude model. The strong excitonic effect pronounced in the optical response of graphene indicates the decreased screening of e-e interactions and zero density of states at the Dirac point [34]. Here we investigated optical residual absorption of graphene at visible and near infrared region. First, the optical response of single layer graphene at the linear dispersion regime was studied theoretically by transfer matrix method. The band to band transition and excitonic effect were included in the model afterwards. Then, details of experiment followed by spectroscopy of optical response of graphene and discussion has been demonstrated.

4.2 Simulation of monolayer graphene

Optical response of a single layer graphene can be deduced using transfer matrix method formulated by Zhan et.al [35]. It is based on the fact that the electric or magnetic fields of two media can be related to each other through transfer matrix. Two types of transfer matrices are transmission matrix and propagation matrix.

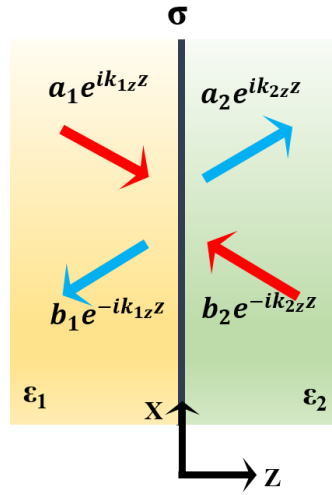


Figure 4.1 Schematic of optical response of monolayer graphene with conductivity of σ sandwiched between two dielectric media with dielectric constants of ϵ_1 and ϵ_2 . Forward and backward propagating electromagnetic waves with field coefficients of a_1 , a_2 , b_1 and b_2 , respectively.

A single layer graphene with optical conductivity σ surrounded by two dielectrics is illuminated with light shown in Figure 4.1. The dielectric constant of the two dielectric media are ϵ_1 and ϵ_2 assuming that light is propagating in z direction.

The connection between fields crosswise the interface is through transmission matrix. When the light is polarized in y direction, the magnetic field for p polarization is the following

$$H_{1y} = (a_1 e^{ik_{1z}z} + b_1 e^{-ik_{1z}z}) e^{ik_{1x}x}, \quad z < 0, \quad 4.1$$

$$H_{2y} = (a_2 e^{ik_{2z}z} + b_2 e^{-ik_{2z}z}) e^{ik_{2x}x}, \quad z > 0 \quad 4.2$$

Where, a_1 and a_2 are field coefficients for the forward propagation while, b_1 and b_2 are correlated to backward propagation. k_{ix} and k_{iz} are x and z components of wave vector $k_i = \sqrt{\epsilon_i} \omega / c$ and, $k_{1x} = k_{2x}$ deducted from Snell's law. Subsequently, electric field \mathbf{E} can be determined from $\hat{\mathbf{E}}_i = -\mu_0 \nu_i (\hat{\mathbf{k}}_i \times \hat{\mathbf{H}}_i)$ presented in equations (4.3) and (4.4). μ_0 is the vacuum permeability and, ν_i is the phase velocity of the electromagnetic wave.

$$\hat{\mathbf{E}}_1 = \frac{a_1}{\epsilon_0 \epsilon_1 \omega} k_{1z} e^{ik_{1z}z} - \frac{b_1}{\epsilon_0 \epsilon_1 \omega} k_{1z} \hat{x} e^{-ik_{1z}z}, \quad z < 0 \quad 4.3$$

$$\hat{\mathbf{E}}_2 = \frac{a_2}{\epsilon_0 \epsilon_2 \omega} k_{2z} e^{ik_{2z}z} - \frac{b_2}{\epsilon_0 \epsilon_2 \omega} k_{2z} e^{-ik_{2z}z}, \quad z > 0 \quad 4.4$$

Where, ϵ_0 is vacuum permittivity. We apply following boundary conditions for electric and magnetic field at $z = 0$ to obtain transmission matrix. The surface normal is $\hat{n} = \hat{z}$.

$$\hat{n} \times (\hat{\mathbf{E}}_2 - \hat{\mathbf{E}}_1) \Big|_{z=0} = 0 \quad 4.5$$

$$\hat{n} \times (\hat{\mathbf{H}}_2 - \hat{\mathbf{H}}_1) \Big|_{z=0} = \hat{\mathbf{J}} \quad 4.6$$

Where \mathbf{J} is the surface current density. By substituting the equations of electric and magnetic fields in boundary condition expressions we are left with following,

$$\frac{k_{2z}}{\varepsilon_2}(a_2 - b_2) - \frac{k_{1z}}{\varepsilon_1}(a_1 - b_1) = 0 \quad 4.7$$

$$(a_1 + b_1) - (a_2 + b_2) = J_x = \sigma E_x \Big|_{z=0} = \frac{\sigma k_{2z}}{\varepsilon_0 \varepsilon_2 \omega} (a_2 - b_2) \quad 4.8$$

Combination of equations (4.7) and (4.8) can connect the field coefficients through the transmission matrix D_{12} as

$$\begin{bmatrix} a_1 \\ b_1 \end{bmatrix} = D_{12} \begin{bmatrix} a_2 \\ b_2 \end{bmatrix} \quad 4.9$$

Where the transition matrix is

$$D_{12} = \begin{bmatrix} 1 + \eta + \xi & 1 - \eta - \xi \\ 1 - \eta + \xi & 1 + \eta - \xi \end{bmatrix} \quad 4.10$$

With the matrix element's parameters as

$$\eta = \frac{\varepsilon_1 k_{2z}}{\varepsilon_2 k_{1z}}, \quad \xi = \frac{\sigma k_{2z}}{\varepsilon_0 \varepsilon_2 \omega}. \quad 4.10$$

In the case of s polarization, electric field is in y direction and the transmission matrix can be calculated as well. Since we study the case of a single layer graphene with two surrounding dielectric media interacting with electromagnetic wave, the transmission matrix is the transfer matrix $M = D_{12}$. Therefore the elements of transfer matrix can yield the reflection coefficient r and transmission coefficient t of a monolayer graphene as

$$r = \frac{M(2,1)}{M(1,1)} \quad , \quad t = \frac{1}{M(1,1)} \quad 4.11$$

Thus the reflectance R and transmittance T will be in the form of,

$$R = |r|^2 \quad , \quad T = \eta |t|^2 \quad 4.12$$

Absorption can be obtained from

$$A = 1 - T - R \quad 4.13$$

Here we consider optical response of single layer graphene in visible and NIR region in which, the optical absorption of graphene is associated with interband transitions. The optical conductivity of pristine graphene is frequency independent in this range and is equal to $\pi e^2/2h$ called universal conductance of graphene where, h is Planck's constant and e is the electron charge. The absorption corresponding to this conductivity is obtained by $A(\omega) = (4\pi / c)\sigma(\omega)$ which equals to $\pi\alpha \approx 2.3\%$. Figure 4.2 demonstrates the transmittance, reflectance and absorptance spectrum of free standing graphene calculated at different Fermi energies. As we expect, the reflectance of graphene shown in Figure 4.2(b) is negligible and absorption is about 2.3%.

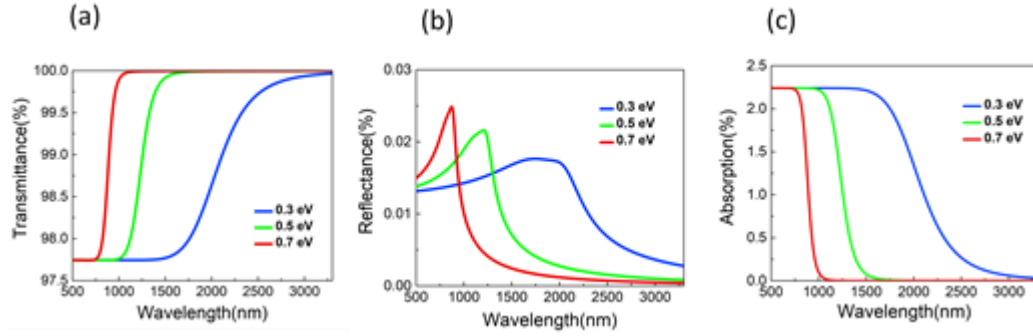


Figure 4.2 Optical response of free standing graphene at different fermi energies. (a) Transmittance of graphene is about 97.7% considering negligible reflectance yields 2.3% absorption. (b) Reflectance spectrum of graphene is inconsiderable and does not have significant effect on the graphene's absorption. (c) Absorption of graphene is about 2.3% in this region.

While Fermi energy of graphene shifts through doping, absorption remains constant. By shifting Fermi energy, the transitions for energy photons below $2E_F$ is not allowed due to Pauli blocking principle. In Figure 4.2, shifting of Fermi energy to higher frequencies is noticeable.

However, the absorption of graphene transferred on a substrate is not 2.3% any longer. Therefore the correction factor $(2/n+1)^2$ should be included. Accordingly, absorption is calculated by $A = \pi\alpha(2/n+1)^2$ where, n is the refractive index of the substrate. Figure 4.3 represents the optical response of graphene on a substrate with refractive index of $n = 1.5$ at different Fermi energies. A simple calculation results in an absorption of 1.47% for this case. The absorption of graphene in our model is around 1.56% which is in close agreement with the theory.

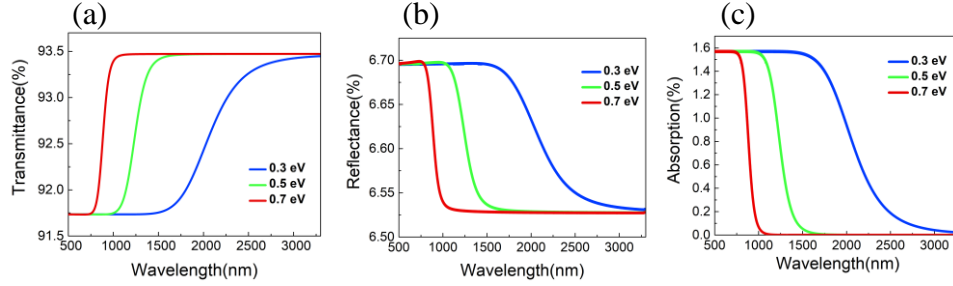


Figure 4.3 Optical spectrum of graphene on a dielectric substrate with refractive index of $n = 1.5$. (a) 91.7% of transmittance is calculated which is decreased compared to the transmittance of free standing graphene. (b) Reflectance is increased to 6.7% and (c) Graphene's absorption is decreased to 1.57% due to refractivity of the substrate.

All the calculations above have been considered near Dirac point where, dispersion relation is linear. In the linear dispersion region, the optical conductivity of graphene is frequency independent and determined by fine structure constant. However the optical conductivity deviates from the universal conductance $\pi e^2/2h$ expected by independent particle model. At higher energy photons, a marked resonance feature is observed which is due to band to band transitions near the M point, the saddle-point singularity of Brillouin zone [34]. The resonance feature at UV is predicted as a symmetric peak at 5.20 eV within independent particle calculations. However the experimental optical conductivity shows an asymmetric peak at 4.62 eV (268 nm). The large redshift of about 600 meV can be explained by taking into account electron-hole interaction role in the optical response of graphene near the M point. Coupling of band to band transition near saddle-point singularity and excitonic effect leads to an asymmetric resonance feature which is in a good agreement with experimental results. Since there is not any analytical expression for interband conductivity of graphene including both resonance feature near saddle-point singularity and excitonic correction, we used the extracted conductivity of graphene from calculated data of reference (34) Figure 4.5 demonstrates the absorption of graphene on the substrate

with refractive index of $n = 1.5$ at higher energy photons and the resonance feature caused by band to band transition near saddle-point and excitonic effect is presented.

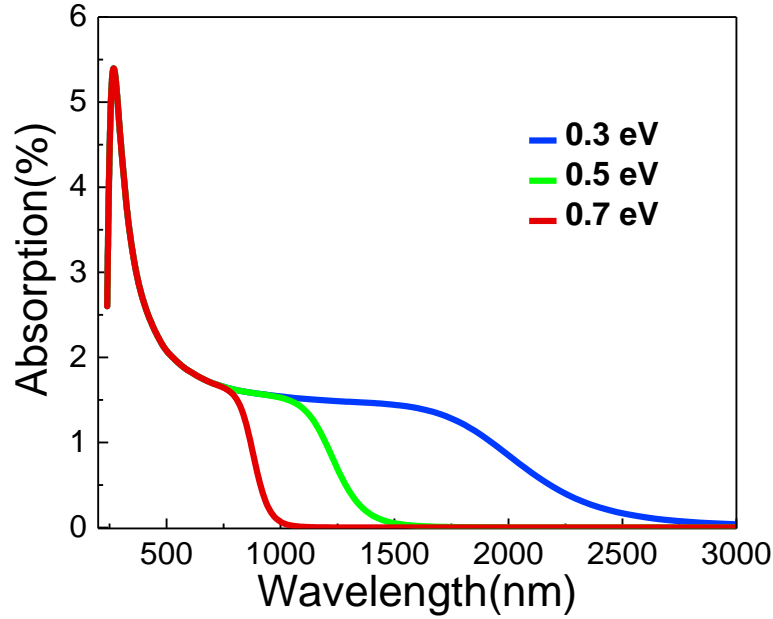


Figure 4.4 Absorption of graphene on quartz substrate for high energy photon region at different Fermi energies. Enhancement of absorption due to interband transitions near M point including excitonic effect is pronounced.

4.3 Experimental results and discussion

In order to observe optical residual absorption of single layer graphene, we utilized a sample consisting of monolayer CVD graphene transferred on quartz substrate. To measure absorption of graphene at different Fermi energies, chemical doping technique is used to introduce additional charge carriers to the graphene layer. By adding electrons to the conduction band of graphene, it is n-doped while introducing holes to its valance band leads to p-doped graphene.

Chemical doping has a different mechanism than electrical doping. Two categories of chemical doping are substitutional doping and surface transfer doping. Substitutional doping of graphene is achieved by replacement of carbon atoms in graphene by dopants which donate either electrons or holes to the graphene. On the other hand, surface transfer doping refers to a post-growth method that charge carriers are distributed at the interface of dopant material and graphene. In this study we applied surface transfer doping method which does not alter the lattice structure of graphene and does not add defects to the graphene. Although, it can add charged impurities to the interface of dopant but the scattering effect due to charge impurities is negligible [36]. In chemical doping method, when the highest occupied molecular orbital of chemical dopant is above graphene's Fermi level, electrons travel from the dopant material to the graphene therefore, dopants behave as a donor and graphene is n-type doped. If the lowest unoccupied molecular orbital is below the graphene's Fermi level, charge carriers transfer from graphene to the dopant. Hence, dopant acts as an acceptor and graphene will be p-doped [37]. Exposure of graphene to donors or acceptors does not improve its mobility however it results in the shift of Dirac point's position in graphene. In this study we exposed graphene to Nitric acid as an acceptor and Ammonia as a donor for p-type and n-type doping, respectively.

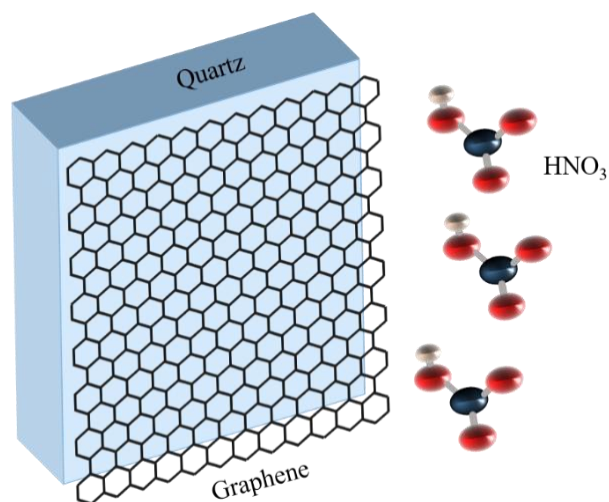


Figure 4.5 The examined sample is CVD grown graphene on quartz where, chemical doping (HNO₃ here) is exploited to shift Fermi energy of graphene. By exposing our sample to nitric acid, we can obtain p-doped graphene.

Varian Cary 5000 UV-Vis-NIR spectrophotometer shown in Figure 4.6 is an instrument which can record data from NIR to UV range and the Varian software running the instrument shows the optical spectrum of sample using recorded data. Its wavelength range is from 175 to 3300 nm established on filtering of particular wavelengths through the sample. It is a dual beam spectrometer where the incident light beam is divided to two beams by a beam splitter. One of the beams passes through the sample while the other one is sent to the reference. The ratio of intensity of light passed through the sample to the intensity of reference beam is referred as transmittance expressed in percentage versus wavelength on the display.

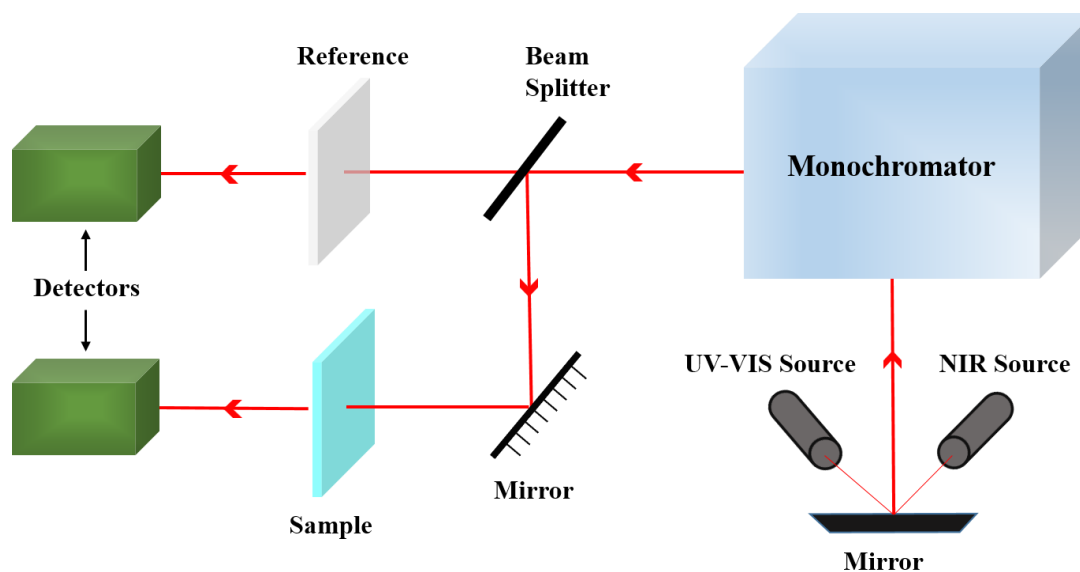


Figure 4.6 Simplified schematic of UV-Vis-NIR spectrophotometer. Light provided by source proceeds to monochromator and the narrow bandwidth outgoing beam of light splits into two beams by beam splitter. One of the beams is transmitted via the reference and the other passes through the sample. The ratio intensity of beams after detection by photo diodes is processed and the spectrum (transmittance vs wavelength) appears on display.

We used Cary 5000 spectrophotometer to measure transmission of monolayer graphene on quartz. The transmittance percentage of graphene at different Fermi energies is illustrated in Figure 4.7 where, quartz is taken as reference. To measure transmittance of graphene at lower wavelengths, we doped graphene by HNO_3 with different time exposures.

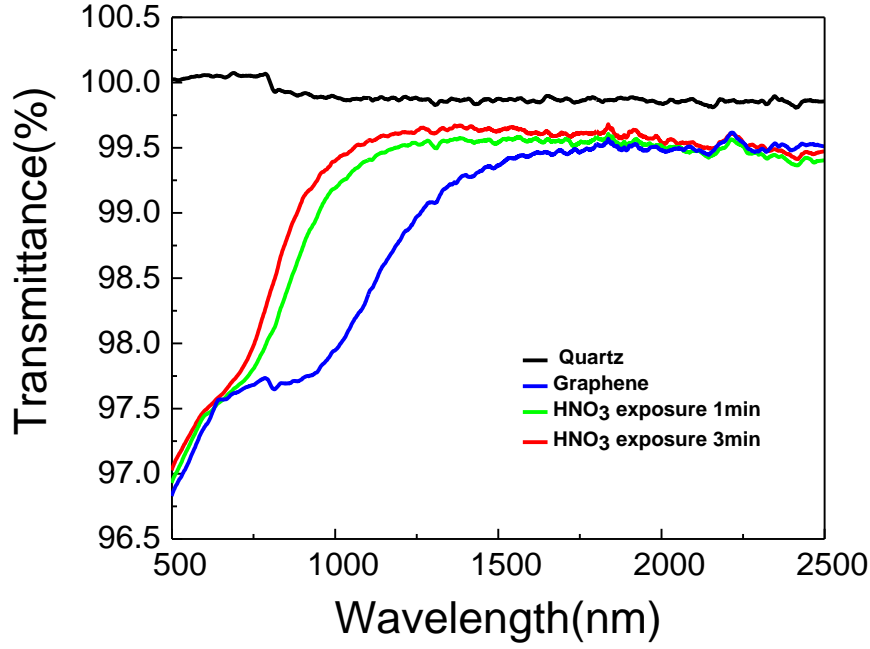


Figure 4.7 Transmission spectrum of graphene on quartz sample exposed to nitric acid. We took quartz as background and measured transmission of graphene. Then by nitric acid exposure in two steps of 1 and 3 minute, transmittance graphene was measured at different Fermi energies.

Because reflectance of graphene at visible-NIR range is negligible, we calculated the absorption by $A = 1 - T$ where, A is absorption and T is transmission. Figure 4.8 indicates normalized absorption of graphene at different Fermi energies. As mentioned before, the absorption in energies less than $2E_F$ known as Pauli blocking regime is expected to be zero although a notable amount of absorption is declared. The residual absorption can be originated from intrinsic or extrinsic sources. Among the former, many-body interactions intensify the frequency dependent scattering rate of charge carriers in the low energy photons regime. Extrinsic effects lead to residual absorption are disorders such as charged impurities and defects. In the visible-NIR region, we measured a residual absorption of 0.5% which can be interpreted in terms

of charged impurities. Chemical residues leads to a finite density of states at the Dirac point which means optical transitions are not blocked effectively therefore, even for energies below $2E_F$, a finite amount of absorption can be found. In addition, by shifting Fermi energy through doping, a slight reduction of residual absorption is observed while the theoretical residual absorption in reference (32) indicated the similar behavior.

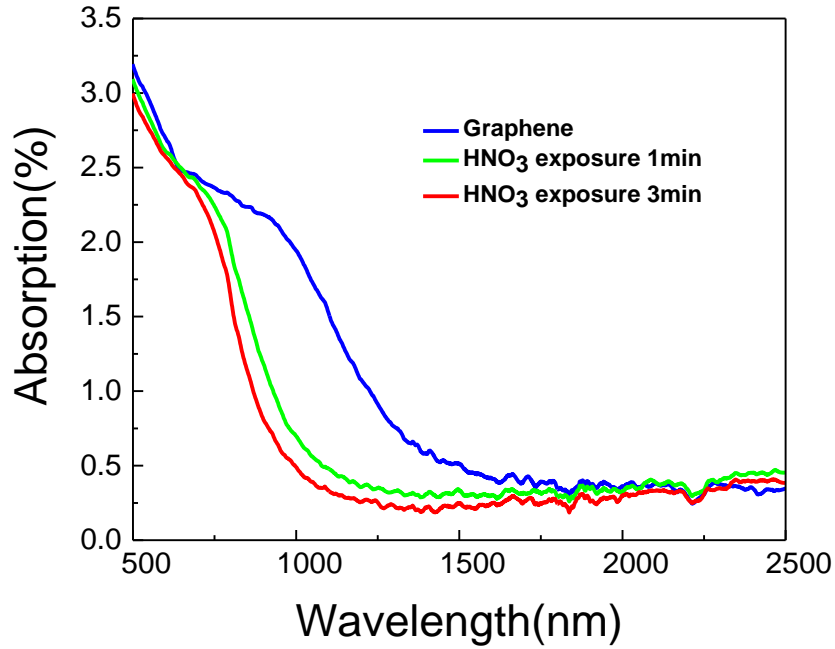


Figure 4.8 Normalized absorption of graphene at different Fermi energies. A finite residual absorption of 0.5% is measured which decreases slightly by increasing the doping level.

To observe optical spectrum of graphene at higher wavelength of NIR region, we doped graphene by ammonia. Figure 4.9 presents transmission of graphene with respect to quartz. By exposing graphene to ammonia, Fermi energy is shifted to lower energies while transmission is about 98.7% for various Fermi energies.

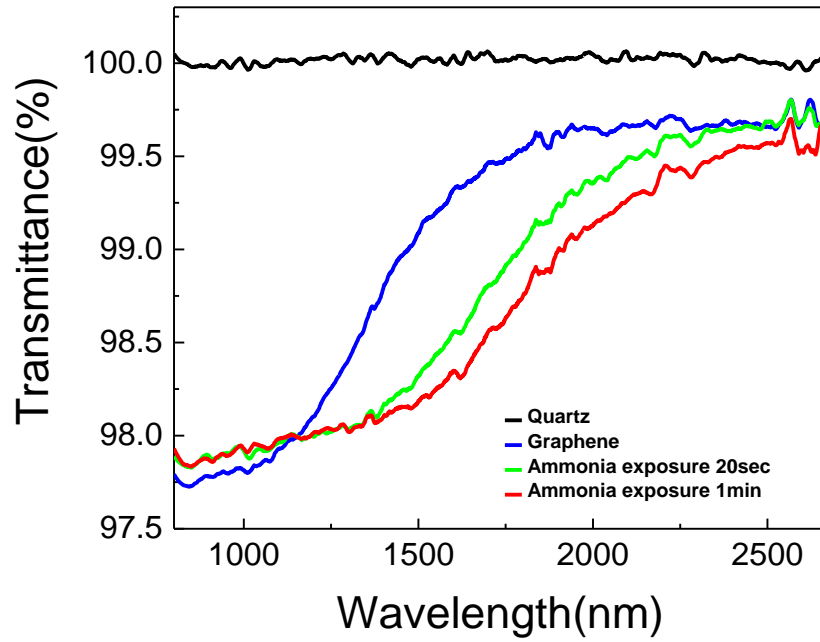


Figure 4.9 Transmittance spectrum of graphene. We took quartz as background and measured transmittance of graphene then exposed it to ammonia to observe transmission of graphene at higher wavelengths.

Normalized absorption of graphene shown in Figure 4.10 deducted from transmittance spectrum demonstrates a constant optical residual absorption of 0.5% while the overall absorption is around 1.7%.

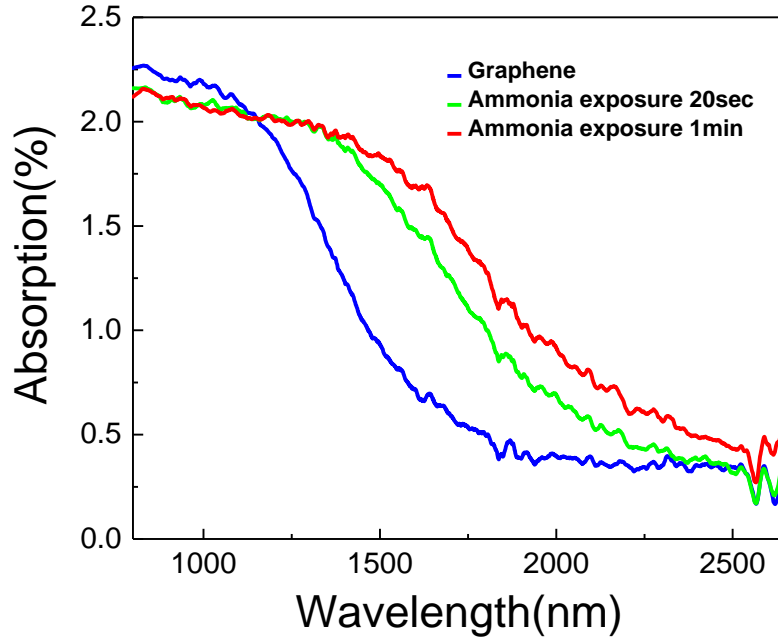


Figure 4.10 Normalized absorption of graphene at lower frequencies in NIR range. Fermi energy is shifting by chemical doping of ammonia to higher wavelengths while the absorption is almost constant and is around 1.7%. The optical residual absorption is 0.5% and is nearly consistent for different Fermi energies.

To extract Fermi energy of graphene associated with different Fermi levels, cut-off wavelengths for the corresponding doping levels have been calculated. Cut-off wavelength equals to twice of Fermi energy due to Pauli blocking principle. As shown in Figure 4.11, in the hole-doped graphene, nitric acid shifts Fermi energy to the higher energy photons while in the electron-doped region, Fermi energy is shifting to lower energy photons.

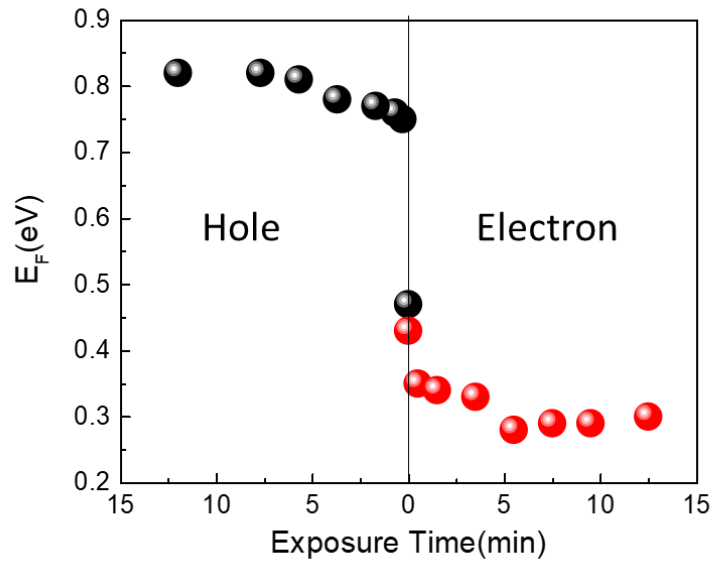


Figure 4.11 Extracted Fermi energies of chemically doped graphene. The hole-doped graphene by nitric acid indicates increasing the Fermi energy while the electron doped part shows the reduction of Fermi energies.

Fermi energies of graphene for both hole and electron chemical doping are determined using Pauli blocking principle in this range. The charge carriers does not show symmetric behavior unlike the electrostatic doping in which charge carriers perform symmetrically.

The optical spectra of graphene transferred layer-by-layer on quartz substrate is shown in Figure 4.12. It appears that optical absorption of graphene is proportional to the number of stacked layers. The optical absorption increases linearly by number of additional layer. In addition, the residual absorption is proportional to the number of layers therefore, it can be speculated that the residual absorption is due to chemical residues left from the wet transferring of graphene on the substrate.

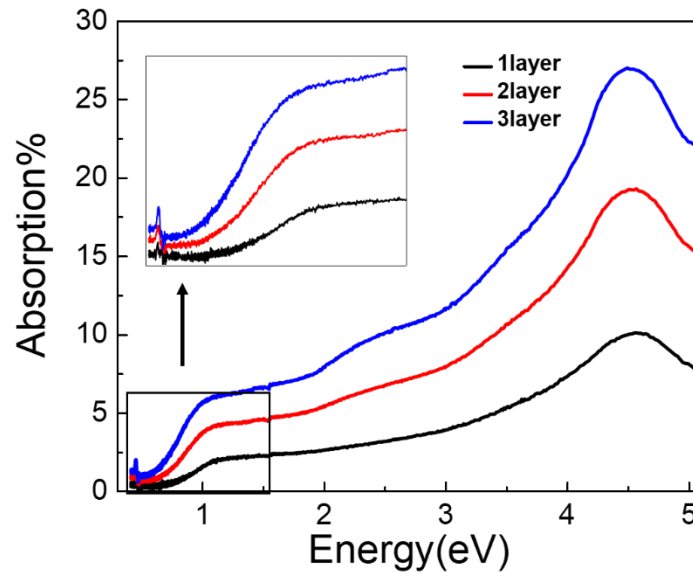


Figure 4.12 Absorption spectra of monolayer, 2layer and 3layer graphene versus energy. The inset shows the visible absorption of stacked layers of graphene.

Absorption spectrum of graphene measured by spectrophotometer as well as calculated one from transfer matrix method are plotted together in figure 4.13 for different Fermi energies. The model fits well with the experimental absorption of graphene in NIR-visible range, however, they do not follow the same trend in UV range which may be due to the variable refractive index of quartz in this range. The experimental absorption of graphene matches with 1.2 layer of graphene in the model because our CVD graphene is not perfectly monolayer.

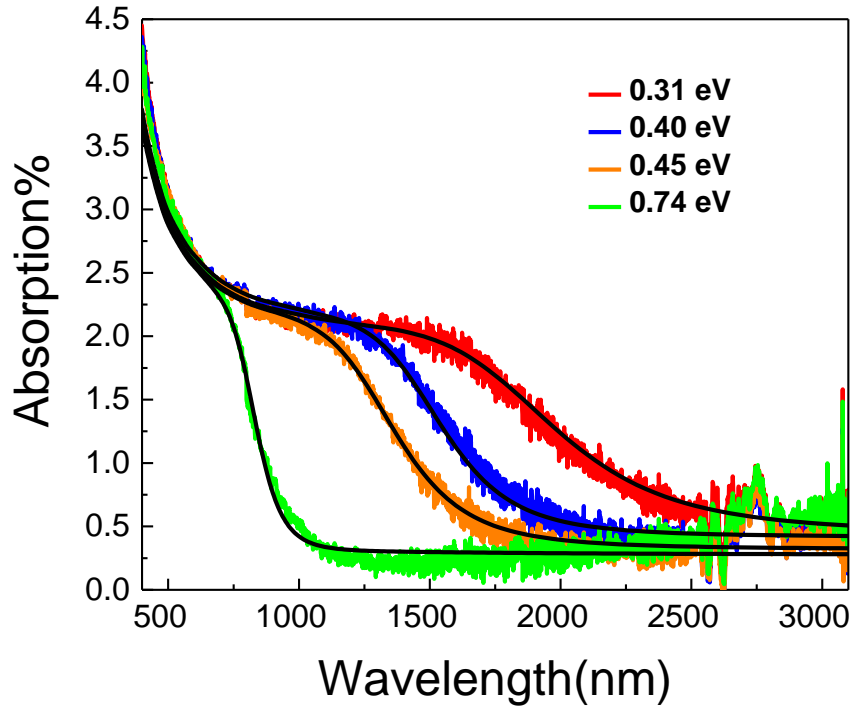


Figure 4.13 Comparison between experimental absorption of graphene with the model at different Fermi energies.

The many body interactions are not incorporated explicitly in the modelling, instead, it is simplified in terms of adding a constant to the real part of interband conductivity for each step of doping. The experimentally measured residual absorption reduces by shifting Fermi level to higher energies while the upper limit of optical absorption is not changing for different doping levels.

Chapter 5

Conclusion

The optical absorption of free standing graphene as an ideal 2D material is $\pi\alpha \approx 2.3\%$. In the case of graphene on a transparent substrate with refractive index of 1.5, the absorption reduces to 1.7% by taking the correction factor into account. It is in good agreement with the universal light absorption of 2D materials which is $1.6 \pm 0.2\%$.

We studied gate-tunable optical properties of graphene from the visible to far infrared region for electron and hole doped regimes. The Fermi energy of graphene was determined by Pauli blocking principle for both electrostatic and chemical doping in visible-NIR range. Charge carriers indicated symmetric behavior for both electron and hole doped regions in electrolyte gating, however, they do not show such a trend for the case of chemical doping.

The optical residual absorption of graphene in visible-NIR range was investigated. The absorption spectra declared that the residual absorption is around 0.5% in this region that reduces moderately when Fermi level is shifted to higher energies. It can be originated from structural disorders in graphene, charged impurities and effects of

many-body interactions. In visible-NIR range, many-body interactions such as electron-phonon coupling or excitonic effect do not have an impact on the optical conductivity of graphene, therefore, the residual absorption can be speculated that is due to charged impurities.

The experimental results are closely in accordance with model in the visible-NIR range and the difference can be due to CVD graphene which may be more than one layer in average.

We conclude by indicating that modeling within independent particle calculations cannot satisfy the experimental optical response of graphene. Numerical calculations such as ab initio GW-Bethe salt peter equation or density functional theory DFT can be used. In addition, utilizing substrates such as hexagonal boron nitride hBN containing less impurities than quartz can be advantageous to find out the role of impurities.

Experiment of stacking layers of graphene indicating the increasing of optical residual absorption by increasing number of layers shows that residual absorption is originated from impurities introduced to graphene during the growth and transfer processes and for pure graphene it will be zero.

Bibliography

- [1] Nair, R.R., P. Blake, A.N. Grigorenko, K.S. Novoselov, T.J. Booth, T. Stauber, N.M.R. Peres, and A.K. Geim, *Fine structure constant defines visual transparency of graphene*. Science, 2008. **320**(5881): p. 1308-1308.
- [2] Mak, K. F., Sfeir, M. Y., Wu, Y., Lui, C. H., Misewich, J. A., & Heinz, T. F. (2008). *Measurement of the Optical Conductivity of Graphene*. *Physical Review Letters*, 101(19).
- [3] Novoselov, K.S., A.K. Geim, S.V. Morozov, D. Jiang, M.I. Katsnelson, I.V. Grigorieva, S.V. Dubonos, and A.A. Firsov, *Two-dimensional gas of massless Dirac fermions in graphene*. Nature, 2005. **438**(7065): p. 197-200.
- [4] Wang, F., Zhang, Y., Tian, C., Girit, C., Zettl, A., Crommie, M., & Shen, Y. R. (2008). *Gate-Variable Optical Transitions in Graphene*. Science, 320(5873), 206-209.
- [5] Mak, K.F., L. Ju, F. Wang, and T.F. Heinz, *Optical spectroscopy of graphene: From the far infrared to the ultraviolet*. Solid State Communications, 2012. **152**(15): p. 1341-1349.
- [6] Li, Z.Q., E.A. Henriksen, Z. Jiang, Z. Hao, M.C. Martin, P. Kim, H.L. Stormer, and D.N. Basov, *Dirac charge dynamics in graphene by infrared spectroscopy*. Nature Physics, 2008. **4**(7): p. 532-535.
- [7] Fox, M. (2016). Optical properties of solids. Oxford: Oxford University Press.
- [8] Fang, H., Bechtel, H. A., Plis, E., Martin, M. C., Krishna, S., Yablonovitch, E., & Javey, A. (2013). *Quantum of optical absorption in two-dimensional semiconductors*. Proceedings of the National Academy of Sciences, 110(29), 11688-11691.
- [9] Chuang, S. L. (2009). Physics of photonic devices (Second ed.). Hoboken, NJ: John Wiley & Sons.
- [10] Wallace, P.R., *The Band Theory of Graphite*. Physical Review, 1947. **71**(9): p. 622-634.
- [11] Bae, S., Kim, H., Lee, Y., Xu, X., Park, J., Zheng, Y., Balakrishnan, J., Lei, T., Ri Kim, H., Song, Y., Kim, Y., Kim, K., Özyilmaz, B., Ahn, J., Hong, B. and Iijima, S. (2010). *Roll-to-roll production of 30-inch graphene films for transparent electrodes*. Nature Nanotechnology, 5(8), pp.574-578.

- [12] Geim, A.K., *Graphene: Status and Prospects*. Science, 2009. **324**(5934): p. 1530-1534.
- [13] Gruneis, A., C. Attaccalite, L. Wirtz, H. Shiozawa, R. Saito, T. Pichler, and A. Rubio, *Tight-binding description of the quasiparticle dispersion of graphite and few-layer graphene*. Physical Review B, 2008. **78**(20).
- [14] Castro Neto, A., Guinea, F., Peres, N., Novoselov, K. and Geim, A. (2009). The electronic properties of graphene. *Reviews of Modern Physics*, 81(1), pp.109-162.
- [15] Geim, A. K., & Novoselov, K. S. (2007). *The rise of graphene*. Nature Materials, 6(3), 183-191.
- [16] Ren, L., Zhang, Q., Yao, J., Sun, Z., Kaneko, R., Yan, Z., Nanot, S., Jin, Z., Kawayama, I., Tonouchi, M., Tour, J. and Kono, J. (2012). *Terahertz and Infrared Spectroscopy of Gated Large-Area Graphene*. *Nano Letters*, 12(7), pp.3711-3715.
- [17] Horng, J., Chen, C., Geng, B., Girit, C., Zhang, Y., Hao, Z., Bechtel, H., Martin, M., Zettl, A., Crommie, M., Shen, Y. and Wang, F. (2011). *Drude conductivity of Dirac fermions in graphene*. *Physical Review B*, 83(16)..
- [18] Novoselov, K., Jiang, D., Schedin, F., Booth, T., Khotkevich, V., Morozov, S. and Geim, A. (2005). *Two-dimensional atomic crystals*. Proceedings of the National Academy of Sciences, 102(30), pp.10451-10453..
- [19] Falkovsky, L. A. (2008). *Optical properties of graphene*. Journal of Physics: Conference Series, 129, 012004.
- [20] Mikhailov, S.A. and K. Ziegler, *New electromagnetic mode in graphene*. Physical Review Letters, 2007. **99**(1).
- [21] Stauber, T., N.M.R. Peres, and A.K. Geim, *Optical conductivity of graphene in the visible region of the spectrum*. Physical Review B, 2008. 78(8).
- [22] Sarma, S. D., Adam, S., Hwang, E. H., & Rossi, E. (2011). *Electronic transport in two-dimensional graphene*. Reviews of Modern Physics, 83(2), 407-470.
- [23] Peres, N. M. (2010). Colloquium: *The transport properties of graphene: An introduction*. Reviews of Modern Physics, 82(3), 2673-2700.
- [24] Li, X., Cai, W., An, J., Kim, S., Nah, J., Yang, D., Piner, R., Velamakanni, A., Jung, I., Tutuc, E., Banerjee, S., Colombo, L. and Ruoff, R. (2009). *Large-Area Synthesis of High-Quality and Uniform Graphene Films on Copper Foils*. *Science*, 324(5932), pp.1312-1314.
- [25] Song, H.S., S.L. Li, H. Miyazaki, S. Sato, K. Hayashi, A. Yamada, N. Yokoyama, and K. Tsukagoshi, *Origin of the relatively low transport mobility*

- of graphene grown through chemical vapor deposition*. Scientific Reports, 2012. **2**.
- [26] Banszerus, L., M. Schmitz, S. Engels, J. Dauber, M. Oellers, F. Haupt, K. Watanabe, T. Taniguchi, B. Beschoten, and C. Stampfer, *Ultrahigh-mobility graphene devices from chemical vapor deposition on reusable copper*. Science Advances, 2015. **1**(6).
 - [27] Kuzmenko, A.B., E. van Heumen, F. Carbone, and D. van der Marel, *Universal optical conductance of graphite*. Physical Review Letters, 2008. **100**(11).
 - [28] M. Liu and X. Zhang, "A high-speed graphene-based broadband modulator," in Frontiers in Optics 2011/Laser Science XXVII, OSA Technical Digest (Optical Society of America, 2011), paper FWG1.
 - [29] Polat, E.O. and C. Kocabas, *Broadband Optical Modulators Based on Graphene Supercapacitors*. Nano Letters, 2013. 13(12): p. 5851-5857.
 - [30] Polat, E.O., O. Balci, and C. Kocabas, *Graphene based flexible electrochromic devices*. Scientific Reports, 2014. 4.
 - [31] Balci, O., E.O. Polat, N. Kakenov, and C. Kocabas, *Graphene-enabled electrically switchable radar-absorbing surfaces*. Nat Commun, 2015. 6.
 - [32] Peres, N. M., Stauber, T., & Neto, A. H. (2008). *The infrared conductivity of graphene on top of silicon oxide*. EPL (Europhysics Letters), 84(3), 38002.
 - [33] Ando, T., Zheng, Y., & Suzuura, H. (2002). *Dynamical Conductivity and Zero-Mode Anomaly in Honeycomb Lattices*. Journal of the Physical Society of Japan, 71(5), 1318-1324.
 - [34] Mak, K. F., Shan, J., & Heinz, T. F. (2011). *Seeing Many-Body Effects in Single- and Few-Layer Graphene: Observation of Two-Dimensional Saddle-Point Excitons*. Physical Review Letters, 106(4).
 - [35] Zhan, T.R., X. Shi, Y.Y. Dai, X.H. Liu, and J. Zi, *Transfer matrix method for optics in graphene layers*. Journal of Physics-Condensed Matter, 2013. **25**(21).
 - [36] Wehling, T. O., Novoselov, K. S., Morozov, S. V., Vdovin, E. E., Katsnelson, M. I., Geim, A. K., & Lichtenstein, A. I. (2008). *Molecular Doping of Graphene*. Nano Letters, 8(1), 173-177.
 - [37] Ristein, J. (2006). *PHYSICS: Surface Transfer Doping of Semiconductors*. Science, 313(5790), pp.1057-1058.